Femtosecond plasmon and photon wave packets excited by a high-energy electron on a metal or dielectric surface

Benjamin J. M. Brenny,[1] Albert Polman,[1,*] and F. Javier García de Abajo[2,3,†]
[1]*Center for Nanophotonics, FOM Institute AMOLF, Science Park 104, 1098 XG Amsterdam, The Netherlands*
[2]*ICFO-Institut de Ciencies Fotoniques, The Barcelona Institute of Science and Technology, 08860 Castelldefels (Barcelona), Spain*
[3]*ICREA-Institució Catalana de Recerca i Estudis Avançats, Passeig Lluís Companys 23, 08010 Barcelona, Spain*
(Received 31 May 2016; published 10 October 2016)

Swift electrons generate coherent transition radiation (TR) when crossing a material surface, as well as surface plasmon polaritons (SPPs) when the material is metallic. We present analytical and numerical calculations that describe the time- and space-dependent electric fields of TR and SPPs induced by 30–300 keV electrons on a Drude metal surface. The generated SPPs form wave packets a few-hundred femtoseconds in duration, depending on the material permittivity. High-frequency components close to the plasmon resonance are strongly damped, causing the wave packets to shift to lower frequencies as they propagate further. TR is emitted to the far field as ultrashort wave packets consisting of just a few optical cycles, with an intensity and angle dependence that is determined by the material permittivity. The excitation reaches its peak amplitude within a few femtoseconds and then drops off strongly for longer times. From a correlation between material permittivity and the calculated emission behavior, we determine qualitative predictions of the TR evolution for any given material. The results presented here provide key insights into the mechanisms enabling swift electrons to serve as nanoscale optical excitation sources.

DOI: 10.1103/PhysRevB.94.155412

I. INTRODUCTION

Electron-beam spectroscopies such as cathodoluminescence (CL) spectroscopy and electron energy-loss spectroscopy (EELS) have gained much attention in nanophotonics research because of their ability to resolve optical excitations with nanometer precision. Just like photons, electrons carry electromagnetic fields, allowing them to optically excite polarizable matter. In fact, due to their short de Broglie wavelengths and correspondingly high momenta, electrons can be used as a highly localized optical excitation source with a spatial resolution unattainable using optical excitation techniques [1–7]. Many advances have been made in the theoretical descriptions of the interactions between electrons and matter that generate radiation [1,8–13]. These electron-light-matter interactions occur on the femtosecond time scale and have only recently been studied in the time domain, in an indirect way, using adapted electron microscopes that combine EELS with synchronized ultrafast optical excitations [14,15]. Most work thus far has focused on exploring the frequency and momentum domains, measuring and simulating spectral responses. Accordingly, analytical theory and simulation techniques have not been applied to investigate the time evolution of CL processes in detail, although time-domain simulation methods have been gaining traction [16,17].

In this article, we develop a theoretical framework to study the radiation excited by swift electrons impinging on a metallic or dielectric surface. We investigate in detail the time evolution of coherent excitation and emission of transition radiation (TR) and surface plasmon polaritons (SPPs). We examine the space, time, and frequency dependence of the electric fields of the moving electron and how they interact with matter to generate radiation. We start by deriving the external fields of an electron in a homogeneous medium, determining the time- and position-dependent behavior of the electric-field components. We then examine an electron impinging on a planar surface, interacting with the medium to induce fields that produce radiation emitted into the far field. The general formalism is derived in frequency and momentum space, after which the time and space dependence is obtained by Fourier transforming the fields. First, we investigate SPPs and study the generation and propagation of these excitations on the femtosecond time scale, for metals described by a Drude dielectric response. We determine the evolution of the SPP wave packet as it propagates away from the point of excitation. We then explore TR, which is composed of far-field emission characterized by ultrashort wave packets that strongly depend on the emission direction. We study both the time and frequency dependence of TR and elucidate the interrelation between the material permittivity and TR emission. This allows us to formulate qualitative predictions of TR emission behavior.

II. ELECTRON EXTERNAL FIELD

A point charge moving with constant velocity in vacuum possesses an electromagnetic field that represents an evanescent source of radiation. Inside a homogeneous medium, the field can be described quite simply, allowing us to study both the time and spectral dependence of the electron field components. We focus on an electron traveling in a straight-line trajectory along the z axis, with a constant velocity vector $\mathbf{v} = v\hat{\mathbf{z}}$, passing by the origin $R = z = 0$ at time $t = 0$. The direction perpendicular to the trajectory is denoted as $\mathbf{R} = R\hat{\mathbf{R}}$, with the position vector defined as $\mathbf{r} = (\mathbf{R}, z)$. The electron charge density is given by $\rho(\mathbf{r},t) = -e\delta(\mathbf{r} - \mathbf{v}t)$. This can be Fourier transformed to ($\mathbf{q}$-ω) space as $\rho(\mathbf{q},\omega) =$

*polman@amolf.nl
†javier.garciadeabajo@icfo.es

$-2\pi e\delta(\omega - \mathbf{q}\cdot\mathbf{v})$. In our derivations, we use Gaussian units and follow the notation used in Ref. [1], but focus only on the electric fields $\mathbf{E}$ (the magnetic field $\mathbf{H}$ can be obtained using the Maxwell-Faraday equation). The equations take into account retardation effects (c is finite and the electron velocity can reach a sizable fraction of c). We also use linear response theory, which assumes that the induced field is linear with the external field of the electron and, consequently, the photon emission probability scales as the square of the external charge ($-e$ for the electron). Maxwell's equations can be solved in momentum-frequency space, leading to the following expression for the electric field of the moving electron:

$$\mathbf{E}(\mathbf{q},\omega) = -\frac{8\pi^2 ie}{q^2 - k^2\epsilon}\left(\frac{k}{c}\mathbf{v} - \frac{\mathbf{q}}{\epsilon}\right)\delta(\omega - \mathbf{q}\cdot\mathbf{v}), \qquad (1)$$

where ϵ is the permittivity of the homogeneous medium and $k = \omega/c$ is the free-space wave number. The momentum $\mathbf{q}$ of the electron field can be decomposed as $\mathbf{q} = (\mathbf{Q}, q_z)$, in components perpendicular ($\mathbf{Q}$) and parallel (q_z) to the trajectory, with $q_z = \omega/v$. The latter expression, which expresses energy conservation for transfers of frequency and wave vector from the electron to the material, is the nonrecoil approximation [1]. It holds for $\hbar q^2/m_e \ll \omega$, which is valid for photon-energy exchanges $\hbar\omega \ll 1$ MeV, as is usually the case in the study of photonic nanostructures. Integrating $\mathbf{E}(\mathbf{q},\omega)$ over the z component of $\mathbf{q}$ results in

$$\mathbf{E}(\mathbf{Q},z,\omega) = \frac{4\pi ie}{v\epsilon}\frac{\mathbf{q} - \mathbf{v}k\epsilon/c}{q^2 - k^2\epsilon}e^{i\omega z/v}. \qquad (2)$$

The electron dispersion $\omega = qv$ lies outside the light cone in free space $\omega = kc$, so the electron does not radiate and the electric field decays exponentially away from the trajectory. In contrast, the electron velocity can exceed the speed of light inside a material, so the electron can couple to excitations in the medium, leading to the emission of Cherenkov radiation; we will not study this here. Performing the Fourier transform over $\mathbf{Q}$ to obtain the electric field in real space, we obtain [1]

$$\mathbf{E}(\mathbf{r},\omega) = \frac{2e\omega}{v^2\gamma_\epsilon\epsilon}e^{i\omega z/v}\left[\frac{i}{\gamma_\epsilon}K_0\left(\frac{\omega R}{v\gamma_\epsilon}\right)\hat{\mathbf{z}} - K_1\left(\frac{\omega R}{v\gamma_\epsilon}\right)\hat{\mathbf{R}}\right], \qquad (3)$$

where $\gamma_\epsilon = 1/\sqrt{1 - \epsilon v^2/c^2}$ is the Lorentz contraction factor and K_m are modified Bessel functions of the second kind [18] (see also Chap. 14 of Ref. [19]). The fields diverge at the origin, so close to the trajectory there is a large contrast in the field strength. Further away from the trajectory, the field amplitude decays with the Bohr cutoff ($v\gamma_\epsilon/\omega$) as a characteristic decay length [1,4]. Using Eq. (3), we can determine the spectral components of the electric field at different points in space. To determine the electric field as a function of time, we Fourier transform Eq. (3) as

$$\mathbf{E}(\mathbf{r},t) = \int\frac{d\omega}{2\pi}\mathbf{E}(\mathbf{r},\omega)e^{-i\omega t}. \qquad (4)$$

Direct numerical integration is used below for the fields produced when the electron crosses an interface. For the swift electron moving in vacuum ($\gamma_\epsilon \to \gamma$), the $E(\mathbf{r},t)$ fields can be determined directly from $\rho(\mathbf{r},t)$ and the Liénard-Wiechert potentials (see pp. 661–665 in Ref. [19]), leading to

$$\mathbf{E}(\mathbf{r},t) = -\frac{\gamma}{[R^2 + \gamma^2(z - vt)^2]^{3/2}}[R\hat{\mathbf{R}} + (z - vt)\hat{\mathbf{z}}]. \qquad (5)$$

For illustration, we study an electron traveling through vacuum, with an energy of 30 keV, corresponding to a velocity of $v = 0.328c = 98.45$ nm fs^{-1}. The results are displayed in Fig. 1, with a schematic of the electron, the coordinate system, and the field orientations as an inset in Fig. 1(a). We present the evanescent decay of the field away from the trajectory of the electron in Fig. 1(a), calculating the total electric-field intensity (time integrated over the entire pulse) as a function of radial distance R, for the two field components E_R and E_z. Notice that the electric field produced by the moving electron diverges at its position, thus reflecting the divergence of the expected value of the electric force that it produces on a test point charge at an arbitrarily small separation from it. Incidentally, this divergence of the real part of the self-interaction is known to be removed by renormalization in the calculation of the Lamb shift [20] or in a proper derivation of the polarizability of a point particle [21]. In CL and EELS, it also disappears because the transition probability is limited to a value given by the imaginary part of the self-interaction [1]. This asymptotic behavior of the fields is clearly visible in Fig. 1(a), with a difference of eight orders of magnitude in the intensity between $R = 1$ nm and $R = 100$ nm. The E_R field component, perpendicular to the trajectory, has a higher intensity than the E_z component. The strong gradient in the field intensity observed here is responsible for the very high excitation resolution of electron-beam spectroscopies.

Figure 1(b) displays the electric-field components as a function of time, for distances $R = 10$ nm and $R = 100$ nm away from the electron trajectory. The E_z component is asymmetric, while the E_R component is symmetric, both displaying a single oscillation. For a distance of $R = 10$ nm, the field transient occurs within $\sim$2 fs, highlighting the extremely short pulse felt by an observer close to the moving electron. At $R = 100$ nm, the field amplitudes have decayed by a factor 100 and the transient spreads out in time by a factor 10. This is due to the fact that further away from the trajectory, the distance between moving electron and observer varies more slowly with time.

Figure 1(c) displays the electric field in the frequency domain. Spectra for the two field components are presented for $R = 10$ nm and the total intensity for $R = 10$ nm and $R = 100$ nm. The different field components display characteristic spectral shapes, with E_z vanishing for small frequencies while E_R has a maximum. At $R = 10$ nm, the spectral range extends well beyond 10 eV; at $R = 100$ nm, the intensity has decayed by a factor 100 and the spectrum is confined to $\sim$1 eV ($\sim$242 THz).

These calculations show that an electron moving through vacuum possesses an electric field that is characterized (at a certain position) by ultrashort pulses, with energies extending beyond 10 eV close to its trajectory. The field strength and spectral content decay when moving further away. Since these fields are evanescent, they cannot couple directly to far-field

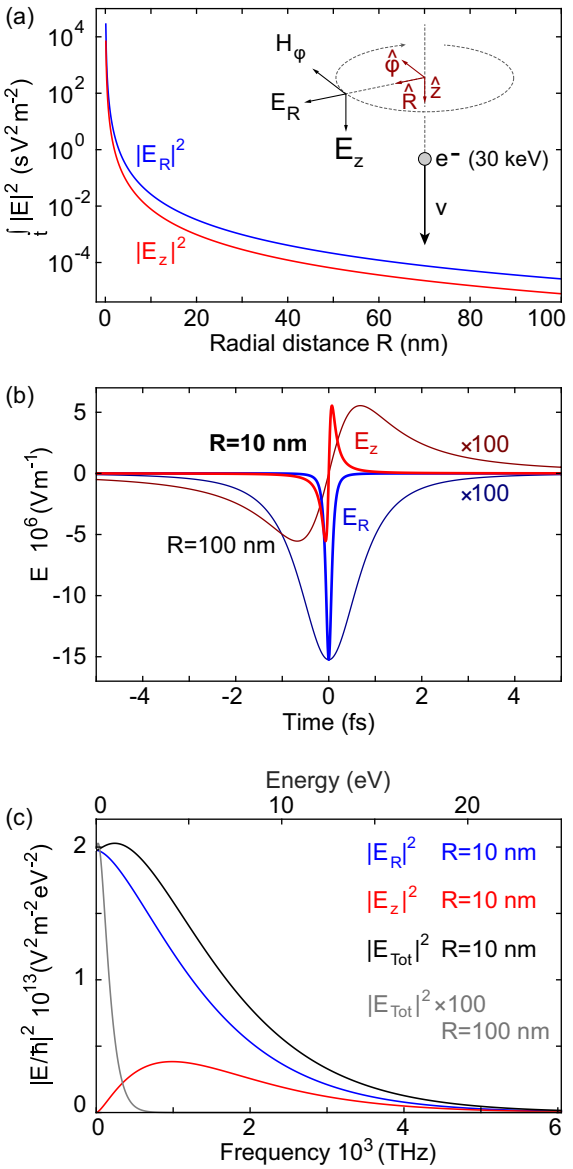

FIG. 1. Electric field produced by a 30 keV electron in vacuum. (a) Total (time-integrated) electric-field intensity of the radial (E_R, in blue) and vertical (E_z, in red) components, as a function of radial distance to the electron trajectory R, displaying the diverging intensity close to the electron trajectory at $R = 0$. The inset depicts a schematic of the moving electron with the coordinate system and orientation of the field components. We evaluate the electric fields for a given radial distance R, height z, and time t or frequency ω. (b) Electric-field amplitudes of the E_R (blue) and E_z (red) components as a function of time, for distances of $R = 10$ nm (thick lines) and $R = 100$ nm (thin lines, amplitudes multiplied by 100), and with the minimum electron-observer distance at $t = 0$. (c) Electric-field intensity in the frequency domain, as a function of frequency and corresponding energy, for the E_R (blue), E_z (red), and E_{tot} (black) components at a distance of $R = 10$ nm, compared to the total intensity for $R = 100$ nm (gray, multiplied by a factor of 100).

radiation. Next, we study an electron impinging on a dielectric medium, leading to processes that can emit radiation.

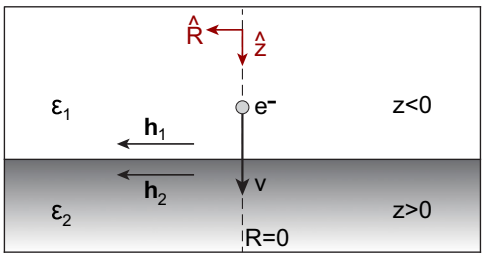

FIG. 2. Schematic of the electron traversing the interface between two media, presenting the coordinate system, as well as the permittivities ϵ_j and surface currents $\mathbf{h}_j$ on either side of the interface.

III. AN ELECTRON IMPINGING ON A PLANAR SURFACE

When an electron reaches and traverses the interface between two media, it generates transition radiation (TR), as well as surface plasmon polaritons (SPPs) in the case of a metal. In general, the electric field can be described by separating the contributions of the external field of the electron in each medium (as if it were an infinite homogeneous medium) and the field that is induced at the surface. The induced field is created by surface charges and currents induced by the approaching electron,

$$\mathbf{E} = \mathbf{E}_j^{\text{ext}} + \mathbf{E}_j^{\text{ind}}.$$

Figure 2 depicts a schematic of the geometry studied here. The induced field can be expressed in terms of the surface currents $\mathbf{h}_j$ as [1,10,22]

$$\mathbf{E}^{\text{ind}}(\mathbf{Q},z,\omega) = \frac{-2\pi k}{q_{zj}} e^{iq_{zj}|z|}\left(\mathbf{h}_j - \frac{1}{k^2\epsilon_j}[\mathbf{Q},\text{sign}(z)q_{zj}] \times \{[\mathbf{Q},\text{sign}(z)q_{zj}]\cdot\mathbf{h}_j\}\right). \quad (6)$$

Here, $q_{zj} = \sqrt{k^2\epsilon_j - Q^2 + i0^+}$, where the square is chosen to yield a positive real part. From the boundary conditions (i.e., the continuity of the $\mathbf{E}$ and $\mathbf{H}$ components parallel to the surface), it follows that the currents only have components of parallel momentum $\mathbf{Q}$ and can be written as $\mathbf{h}_j = D\mu_j\hat{\mathbf{Q}}$. The induced electric field takes the form

$$\mathbf{E}_j^{\text{ind}}(\mathbf{Q},z,\omega) = \frac{2\pi}{k\epsilon_j} D\mu_j e^{\text{sign}(z)iq_{zj}z}[-q_{zj}\hat{\mathbf{Q}} + \text{sign}(z)Q\hat{\mathbf{z}}], \quad (7)$$

where

$$D = \frac{2ieQ/c}{\epsilon_1 q_{z2} + \epsilon_2 q_{z1}}, \quad (8)$$

$$\mu_1 = \frac{\epsilon_1 q_{z2} - \epsilon_1\omega/v}{q^2 - k^2\epsilon_2} - \frac{\epsilon_1 q_{z2} - \epsilon_2\omega/v}{q^2 - k^2\epsilon_1}, \quad (9)$$

and

$$\mu_2 = \frac{\epsilon_2 q_{z1} + \epsilon_1\omega/v}{q^2 - k^2\epsilon_2} - \frac{\epsilon_2 q_{z1} + \epsilon_2\omega/v}{q^2 - k^2\epsilon_1}. \quad (10)$$

We can now combine the external and reflected fields together to obtain the complete expressions for the electron electric fields on both sides of the interface, for both field

components. Recall from Eq. (2) that the external field contains components $\mathbf{q} - \mathbf{v}k\epsilon/c$, with $\mathbf{q} = (\mathbf{Q},\omega/v)$. We obtain the following expressions for $\mathbf{E}(\mathbf{Q},z,\omega) = \mathbf{E}_R + \mathbf{E}_z = E_R\hat{\mathbf{Q}} + E_z\hat{\mathbf{z}}$:

$$E_R = \frac{4\pi i e}{v\epsilon_1}\frac{Q}{q^2 - k^2\epsilon_1}e^{i\omega z/v} - \frac{2\pi}{k\epsilon_1}q_{z1}D\mu_1 e^{-iq_{z1}z}, \quad z < 0 \tag{11a}$$

$$E_z = \frac{4\pi i e}{v\epsilon_1}\frac{\frac{\omega}{v}\left(1 - \frac{v^2}{c^2}\epsilon_1\right)}{q^2 - k^2\epsilon_1}e^{i\omega z/v} - \frac{2\pi}{k\epsilon_1}QD\mu_1 e^{-iq_{z1}z}, \quad z < 0 \tag{11b}$$

$$E_R = \frac{4\pi i e}{v\epsilon_2}\frac{Q}{q^2 - k^2\epsilon_2}e^{i\omega z/v} - \frac{2\pi}{k\epsilon_2}q_{z2}D\mu_2 e^{iq_{z2}z}, \quad z > 0 \tag{11c}$$

$$E_z = \frac{4\pi i e}{v\epsilon_2}\frac{\frac{\omega}{v}\left(1 - \frac{v^2}{c^2}\epsilon_2\right)}{q^2 - k^2\epsilon_2}e^{i\omega z/v} + \frac{2\pi}{k\epsilon_2}QD\mu_2 e^{iq_{z2}z}, \quad z > 0. \tag{11d}$$

In order to obtain the fields as a function of space and time, we Fourier transform back from ($\mathbf{Q}$-ω) space:

$$\mathbf{E}(\mathbf{r},t) = \int \frac{d^2\mathbf{Q}}{(2\pi)^2}e^{i\mathbf{Q}\cdot\mathbf{R}}\int \frac{d\omega}{2\pi}e^{-i\omega t}\mathbf{E}(\mathbf{Q},z,\omega). \tag{12}$$

The integral over $\mathbf{Q}$ can be partially simplified by removing the azimuthal component of $\mathbf{Q}$ to leave only the radial part, so that we obtain a single integral over Q. This approach differs between the two field components, since $\mathbf{E}_z$ contains no vectorial component of $\mathbf{Q}$, but $\mathbf{E}_R$ does. We find for $\mathbf{E}_z$ that

$$\int \frac{d^2\mathbf{Q}}{(2\pi)^2}e^{i\mathbf{Q}\cdot\mathbf{R}} = \int_0^\infty \frac{Q}{2\pi}dQJ_0(QR),$$

while for $\mathbf{E}_R$,

$$\int \frac{d^2\mathbf{Q}}{(2\pi)^2}e^{i\mathbf{Q}\cdot\mathbf{R}}\hat{\mathbf{Q}} = \int_0^\infty \frac{Q}{2\pi}dQiJ_1(QR)\hat{\mathbf{R}}.$$

We apply these identities to Eq. (12), and further use causality [$E(\omega) = E^*(-\omega)$], to reduce the fields to

$$\mathbf{E}_z(\mathbf{r},t) = \int_0^\infty \frac{Q}{2\pi}dQJ_0(QR)\int_0^\infty \frac{d\omega}{\pi}\mathrm{Re}\{e^{-i\omega t}\mathrm{E}_z(Q,z,\omega)\}\hat{\mathbf{z}}, \tag{13a}$$

$$\mathbf{E}_R(\mathbf{r},t) = \int_0^\infty \frac{Q}{2\pi}dQJ_1(QR) \times \int_0^\infty \frac{d\omega}{\pi}\mathrm{Im}\{-e^{-i\omega t}\mathrm{E}_R(Q,z,\omega)\}\hat{\mathbf{R}}, \tag{13b}$$

where $E_z(Q,z,\omega)$ and $E_R(Q,z,\omega)$ are given by Eq. (11). Now that we have derived this general formalism, these integrals can be solved numerically to study SPP and TR generation. From these equations, we can derive analytical expressions for the electric-field components in the far field. We demonstrate this in the following sections.

IV. SURFACE PLASMON POLARITONS

The excitation of surface plasmon polaritons by fast electrons was discovered several decades ago [23–25] and has since been demonstrated in a broad variety of experiments [2,26–28]. In studying the excitation of SPPs, we can ignore the external electric field as it decays evanescently and thus does not generate radiation. In our formalism, plasmons are revealed by the induced electric fields [Eq. (7)] and, more specifically, they originate in the pole of the denominator of D: $\epsilon_1 q_{z2} + \epsilon_2 q_{z1} = 0$. This equation leads to the plasmon dispersion relation,

$$Q_{\mathrm{SPP}} = k\sqrt{\frac{\epsilon_1\epsilon_2}{\epsilon_1 + \epsilon_2}}. \tag{14}$$

We now use the plasmon-pole approximation [1,10,29], retaining only the contribution of the plasmon pole at $Q = Q_{\mathrm{SPP}}$. For large distances ($R \gg \lambda$), one can perform the integral over Q from Eq. (13), allowing us to derive analytical expressions for the fields of the SPPs. Using this method, D becomes

$$D \approx \frac{C}{Q - Q_{\mathrm{SPP}}}, \tag{15}$$

where the denominator arises from a Taylor expansion around the plasmon pole,

$$\epsilon_1 q_{z2} + \epsilon_2 q_{z1} \approx -Q_{\mathrm{SPP}}\left(\frac{\epsilon_1}{q_{z2}} + \frac{\epsilon_2}{q_{z1}}\right)(Q - Q_{\mathrm{SPP}}) = \frac{(Q - Q_{\mathrm{SPP}})}{A},$$

leading to

$$C = \frac{2ei\,QA}{c}.$$

To determine the SPP electric fields in space as a function of frequency, we can rewrite the frequency-domain part of Eq. (13), making the plasmon pole explicit, and perform the integral over Q,

$$\mathbf{E}_{\mathrm{SPP}}(\mathbf{r},\omega) \propto \int_0^\infty dQJ_m(QR)\frac{f(Q,z,\omega)}{Q - Q_{\mathrm{SPP}}} \approx 2\pi\frac{i}{2}f(Q_{\mathrm{SPP}},z,\omega)H_m^{(1)}(Q_{\mathrm{SPP}}R), \tag{16}$$

where $H_m^{(1)}$ is a Hankel function of the first kind. By combining Eq. (16) with Eq. (11), we can consolidate an expression for the frequency-dependent SPP fields in a relatively compact way, and find

$$\mathbf{E}_{\mathrm{SPP}}(\mathbf{r},\omega) = \frac{2\pi ei\,AQ_{\mathrm{SPP}}^2}{ck\epsilon_j}\mu_j e^{\mathrm{sign}(z)iq_{zj}z}\left[\mathrm{sign}(z)i\,Q_{\mathrm{SPP}} \times H_0^{(1)}(Q_{\mathrm{SPP}}R)\hat{\mathbf{z}} + q_{zj}H_1^{(1)}(Q_{\mathrm{SPP}}R)\hat{\mathbf{R}}\right]. \tag{17}$$

This equation is applicable on both sides of the interface that the electron traverses. As in the previous section, the final step to obtain the time-dependent electric fields is to Fourier transform over the frequency domain,

$$\mathbf{E}_{\mathrm{SPP}}(\mathbf{r},t) = \int_0^\infty \frac{d\omega}{\pi}\mathrm{Re}\{\mathbf{E}_{\mathrm{SPP}}(\mathbf{r},\omega)e^{-i\omega t}\}. \tag{18}$$

We calculate the time- and frequency-dependent SPP electric fields for a 30 keV electron impinging on a Drude metal under normal incidence, with a permittivity described by

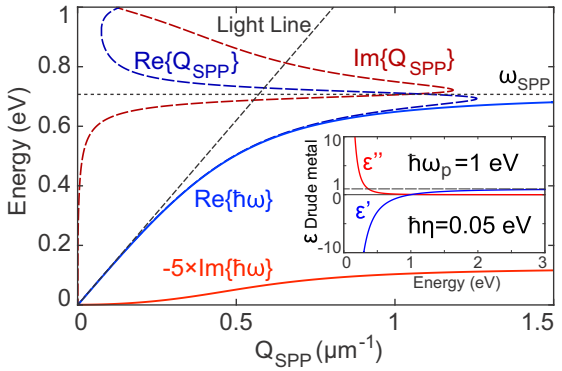

FIG. 3. Dispersion relation of surface plasmon polaritons (SPPs) for a Drude metal with $\hbar\omega_p = 1$ eV and $\hbar\eta = 0.05$ eV, displaying the energy as a function of the SPP wave vector $Q_{\rm SPP}$. Real (imaginary) parts are represented as blue (red) curves for both complex $Q_{\rm SPP}$ (dashed curves for $\mathrm{Re}\{Q_{\rm SPP}\}$ and $\mathrm{Im}\{Q_{\rm SPP}\}$, as a function of real energy in the vertical axis) and complex ω (solid curves for $\mathrm{Re}\{\hbar\omega\}$ and $-5 \times \mathrm{Im}\{\hbar\omega\}$, as a function of real wave vector in the horizontal axis). The diagonal dashed line denotes the light cone, while the horizontal one indicates the energy of the SPP resonance frequency $\omega_{\rm SPP}$. The inset depicts the permittivity ϵ of the Drude metal as a function of energy.

$\epsilon(\omega) = \epsilon_{\rm D}(\omega) = \epsilon_0 - \omega_{\rm p}^2/(\omega^2 + i\eta\omega)$. The Fourier transform is performed numerically by summing over energies in the range $\hbar\omega = 10^{-6} - 100$ eV, divided into 10^6 steps. We choose $\hbar\omega_{\rm p} = 1$ eV and $\hbar\eta = 0.05$ eV. The corresponding plasmon-dispersion relation is depicted in Fig. 3, the SPPs being excited for frequencies $\omega \leqslant \omega_{\rm SPP} = \omega_{\rm p}/\sqrt{2}$. We show representations of both complex frequency and complex wave vector in the dispersion relation.

The representation with real wave vector and complex frequencies is well suited for pulsed excitations (i.e., such that a single frequency is not well defined), in which the imaginary part of the complex frequency describes the decay in time [30]. In contrast, a quasimonochromatic, spatially delocalized excitation is better represented by the real-frequency description, in which the imaginary part of the complex wave vector accounts for propagation losses. These two representations are very similar along most of the dispersion curve, except near the SPP horizontal asymptote, where the complex wave-vector picture describes a band bending followed by negative dispersion, while the complex frequency picture fully retains the asymptotic behavior. For the electron incident on a planar surface, both representations are equivalent, depending on which of the integrals (ω or Q) is performed earlier in Eq. (12). In the expression of Eq. (18), the frequency remains real, as we have chosen to carry out the wave-vector integral first. The $\mathrm{Im}\{\omega\}$ term is negative (as expected for $e^{-i\omega t}$ to decay for $t \to \infty$), so we multiply it by -5 to show it on the same scale as the other quantities.

Figure 4(a) shows the time evolution of an SPP wave packet, as observed for a height $z = -10$ nm above the metal surface, at a radial distance $R = 10$ μm from the electron trajectory ($R \gg \lambda$). After ∼30 fs, we clearly observe an increase in amplitude and an oscillating wave packet that then decays, for both field components. As expected for the

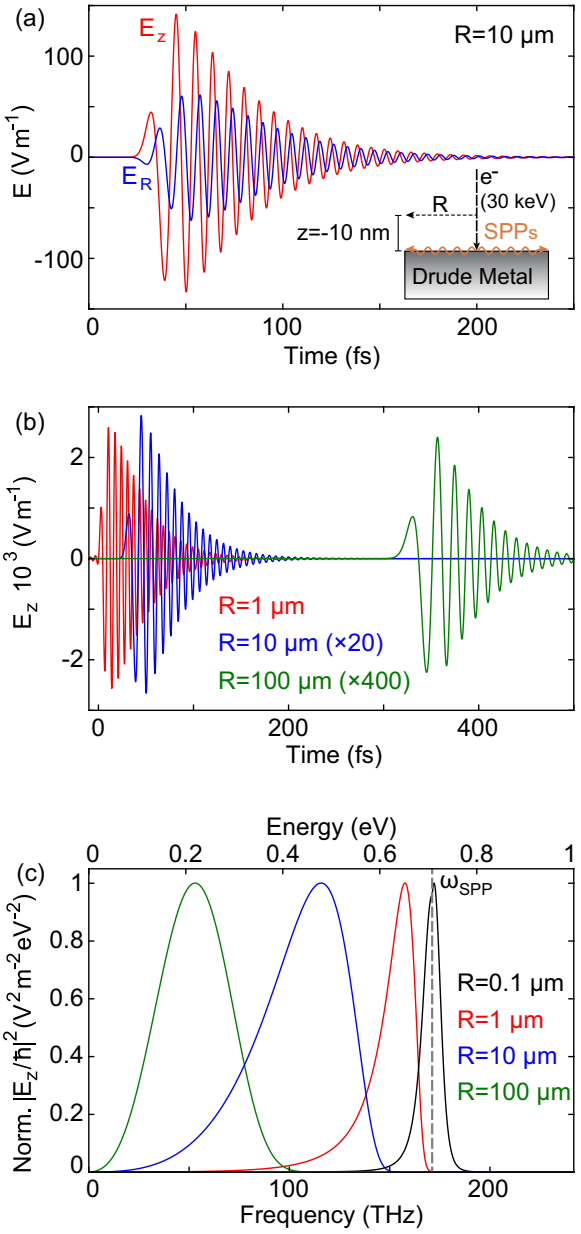

FIG. 4. Electric field of surface plasmon polaritons (SPPs) excited by a 30 keV electron, propagating along the surface of a Drude metal (same parameters as in Fig. 3). (a) Electric-field amplitudes of the SPP wave packet, showing the E_R (blue) and E_z (red) components as a function of time, evaluated for a height 10 nm above the metal surface and a distance $R = 10$ μm away from the electron impact position (see inset). The time $t = 0$ corresponds to the electron crossing the interface. (b) Comparison of the E_z SPP amplitude as a function of time for a fixed height $z = -10$ nm at different distances of 1 μm (red), 10 μm (blue, multiplied by 20), and 100 μm (green, multiplied by 400). (c) Comparison of the intensities of the E_z SPP field component in the frequency domain, each normalized to the maximum value at the same distances as in (c). Data for $R = 0.1$ μm (in black) are also presented. The SPP resonance frequency $\omega_{\rm SPP}$ is indicated.

transverse-magnetic (TM) polarized SPPs, E_z oscillates with larger amplitude than E_R. The wave packet has a duration of a few-hundred femtoseconds, and considering the distance R and the time of the onset, is propagating close to the

speed of light. This is to be expected at large distances and times, as the lowest-frequency components close to the light line propagate with the lowest loss and the slower, high-frequency components are strongly damped; see both $\mathrm{Im}\{\hbar\omega\}$ and $\mathrm{Im}\{Q_{\mathrm{SPP}}\}$ in Fig. 3. In Fig. S1 of the Supplemental Material [31], we present the full time evolution and spectral behavior over a 60 μm range.

In Fig. 4(b), we compare the time evolution of the SPP wave packet at $R = 1$, 10, and 100 μm. The period of the oscillations in the wave packet increases for further distances, corresponding to the shift to lower frequencies. The wave packet reaches its maximum amplitude within a single optical cycle, as expected for the single-cycle excitation; see Fig. 1(b). It then decays within ∼200 fs after the initial onset, the duration determined by the damping rate η. In Fig. S2 of the Supplemental Material [31], we compare the SPP wave-packet evolution for different material parameters and electron energies. Essentially, the electromagnetic field oscillates in time with a characteristic period $\sim 1/\omega_p$, and therefore all the results reported here can be scaled appropriately for other values of the plasma frequency. The attenuation introduced through η affects the temporal extension of the field (increasing $|\mathrm{Im}\{\omega\}|$) and, consequently, also the number of oscillations that can be resolved.

To compare the time evolution to the spectral behavior, we calculate the frequency-dependent fields in Fig. 4(c), where data for a distance of $R = 100$ nm are also used. All spectra have been normalized to their maximum: 5.1×10^{12}, 5.7×10^{9}, 7.4×10^{6}, and 2.3×10^{4} $\mathrm{V^2\ m^{-2}\ eV^{-2}}$ for $R = 0.1$, 1, 10, and 100 μm, respectively. Close to the electron trajectory, for $R = 100$ nm, the SPP spectrum is very sharp and peaks at ω_{SPP}. For larger distances, the spectrum broadens and shifts to lower frequencies, as expected from the frequency-dependent damping discussed above.

V. TRANSITION RADIATION

Transition radiation (TR) is a common form of radiation excited by an electron interacting with matter, as it occurs for any swift electron (or charged particle) crossing the boundary between two different media [32–36]. A simple and intuitive way to view TR is that the electromagnetic fields of the electron are "in equilibrium" with their environment, obeying the equations for a homogeneous medium outlined above. If the two media are different, however, the fields of the electron must have adjusted to the new electromagnetic properties of the second material. This modification of the fields as the electron transitions between the media is then accompanied by radiation. Jackson describes TR as portions of the electromagnetic field that must shake it off as radiation (see pp. 646–654 in Ref. [19]). An alternate intuitive explanation is provided by the method of image charges. The negatively charged electron produces a positive image charge below the surface, inducing an effective dipole normal to the surface which vanishes and radiates when the electron passes through the interface. This problem can be treated by describing the field lines of two moving charges of opposite sign that instantaneously stop (at the interface) or start (moving away from the interface) [37–39]. More generally, the approaching electron induces surface charges and currents which polarize the atoms in the material close to the trajectory. These polarization charges react and create an induced field which can radiate out to the far field as transition radiation.

The emission actually must originate from the induced field, just as for SPPs, since the homogeneous fields decay evanescently away from the trajectory of the moving electron and do not couple directly to far-field radiation, so we can discount them in the derivation of the TR fields. Using the general formalism derived for the single interface, we can write the $\mathbf{E}(\mathbf{r},\omega)$ fields, taking only the integral over Q from Eq. (12) applied to the components of Eq. (11):

$$\mathbf{E}(\mathbf{r},\omega) = \int_0^\infty \frac{Q}{2\pi} dQ \frac{2\pi}{k\epsilon_j} D\mu_j e^{iq_{z1}|z|} \times [J_0(QR)\mathrm{sign}(z)Q\hat{\mathbf{z}} - iJ_1(QR)q_{zj}\hat{\mathbf{R}}]. \quad (19)$$

TR is emitted to the far field, so taking the limit for large distances, $kr \longrightarrow \infty$, we can evaluate the integral over Q for the two different field components. Here we examine only the upper hemisphere ($z < 0$, see Fig. 2), taken to be vacuum:

$$\int_0^\infty dQ J_0(QR) e^{iq_{z1}|z|} f(Q) \approx -i\frac{q_{z1}}{Q}\frac{e^{ikr}}{r} f(Q), \quad (20a)$$

$$\int_0^\infty dQ J_1(QR) e^{iq_{z1}|z|} f(Q) \approx -\frac{q_{z1}}{Q}\frac{e^{ikr}}{r} f(Q), \quad (20b)$$

where the value of Q in the right-hand side of the equation is determined by the emission direction (see below). Applying this approximation to Eq. (19) leads to a compact expression for the spectral components of the TR electric field:

$$\mathbf{E}_{\mathrm{TR}}(\mathbf{r},\omega) = i\frac{q_{z1}}{k} D\mu_1 \frac{e^{ikr}}{r}(Q\hat{\mathbf{z}} + q_{zj}\hat{\mathbf{R}}). \quad (21)$$

The fields for the lower hemisphere can be obtained by analogy, using the corresponding components from Eq. (11). Making use of the geometrical relations between R, z, and r as well as Q, q_{z1}, and k, we can define an angle θ that determines the emission direction with respect to the surface normal: $\cos\theta = q_{z1}/k = z/r$ and $\sin\theta = Q/k = R/r$. Making use of these relations, we can rewrite the vectorial part of Eq. (21) as

$$(Q\hat{\mathbf{z}} + q_{zj}\hat{\mathbf{R}}) = k\left(\frac{R}{r}\hat{\mathbf{z}} + \frac{z}{r}\hat{\mathbf{R}}\right) = k\hat{\theta}.$$

This helps to further simplify Eq. (21), which reduces to

$$\mathbf{E}_{\mathrm{TR}}(\mathbf{r},\omega) = iq_{z1} D\mu_1 \frac{e^{ikr}}{r}\hat{\theta}. \quad (22)$$

We can rewrite this with a more explicit dependence on θ, finding a result very similar to that for the magnetic field as derived in Ref. [1]:

$$\mathbf{E}_{\mathrm{TR}}(r,\theta,\omega) = ik\cos\theta D\mu_1 \frac{e^{ikr}}{r}\hat{\theta}. \quad (23)$$

We can evaluate this expression for $Q = k\sin\theta$. The asymptotic part $f(Q)$ of Eq. (20) can be used to obtain the TR emission probability by integrating over the upper hemisphere, leading to

$$\Gamma_{\mathrm{TR}}(\omega) = \frac{1}{2\pi\hbar k}\int_0^{\pi/2} \sin\theta d\theta |k\cos\theta D\mu_1|^2. \quad (24)$$

Finally, Eq. (23) can also be used to determine the TR electric field as a function of time by performing the Fourier transform over frequency,

$$\mathbf{E}_{\mathrm{TR}}(r,\theta,t) = \int_0^\infty \frac{d\omega}{\pi} \mathrm{Re}\{\mathrm{E}_{\mathrm{TR}}(r,\theta,\omega)e^{-i\omega t}\}\hat{\theta}. \quad (25)$$

For a nondispersive medium, this can be simplified even further, since there are no longer any frequency-dependent components except for the $e^{-i\omega t}$ term. The integral over ω then results in a $\delta(r-ct)$ term. In particular, for a perfect electric conductor, the TR electric field in space and time reduces to [38]

$$\mathbf{E}_{\mathrm{TR}}(r,\theta,t) = \frac{2ev\sin\theta}{rc} \frac{\delta(r-ct)}{1-\left(\frac{v}{c}\right)^2\cos^2\theta}\hat{\theta}. \quad (26)$$

We evaluate Eq. (25) numerically, since it is generally applicable for any material. We use a fixed distance $r_0 = \sqrt{2}$ μm from the origin (so that $-z = R = 1$ μm for $\theta = 45°$) for different combinations of R and z to obtain a suitable distribution of angles θ. We use a 30 keV electron impinging on the same Drude metal as for the SPP calculation, with $\hbar\omega_p = 1$ eV and $\hbar\eta = 0.05$ eV, summing over energies in the range $\hbar\omega = 10^{-6} - 100$ eV, divided into 10^6 steps. We find that a large range of energies is necessary to obtain good convergence ($\hbar\omega \sim 100$ eV), although the main features are resolved even with a smaller range ($\hbar\omega \sim 10$ eV). These values are, however, related to the energy/frequency dependence of the material permittivity. The larger the range in frequencies over which ϵ displays features, the larger the range needed in the calculation for good convergence.

Figure 5 displays the results of these time-resolved calculations. Figure 5(a) presents the TR electric-field intensity (on a log scale) as a function of the emission angle θ and normalized time $T = t - r_0/c$. Radiation emitted at the instant the electron traverses the interface will reach the position of the observer (at a distance r_0) at the time $T = 0$, at which a sharp increase in intensity is observed for all angles. Just as for the SPPs, TR forms a very short electromagnetic wave packet that travels through space. Comparing different angles, we clearly observe different regimes. For angles up to ~60°, there are distinct oscillations in the intensity, which propagate longer at lower angles. For angles above ~60°, we no longer see these oscillations, but instead see a uniform decay in intensity.

To study the time evolution in more detail, we directly compare the time trace for different angles (denoted by the horizontal white dashed lines), showing the TR electric-field amplitude on a linear scale, in Fig. 5(b). The inset depicts a schematic of the process, with the simple model of the negatively charged electron inducing a positive mirror charge that creates a vertical dipole. Indeed, the angular emission pattern of TR displays two lobes (representing a cross cut through a toroidal three-dimensional pattern), similar to the emission from a vertical point dipole above the interface. Examining the TR wave packets, it is obvious that for all angles there is no discernible emission before $T = 0$. The radiation only begins at $T = 0$, rising rapidly to a maximum within a few femtoseconds, before decaying within ~30 fs (for the material parameters used here). TR thus consists of extremely short-lived wave packets. Comparing the different

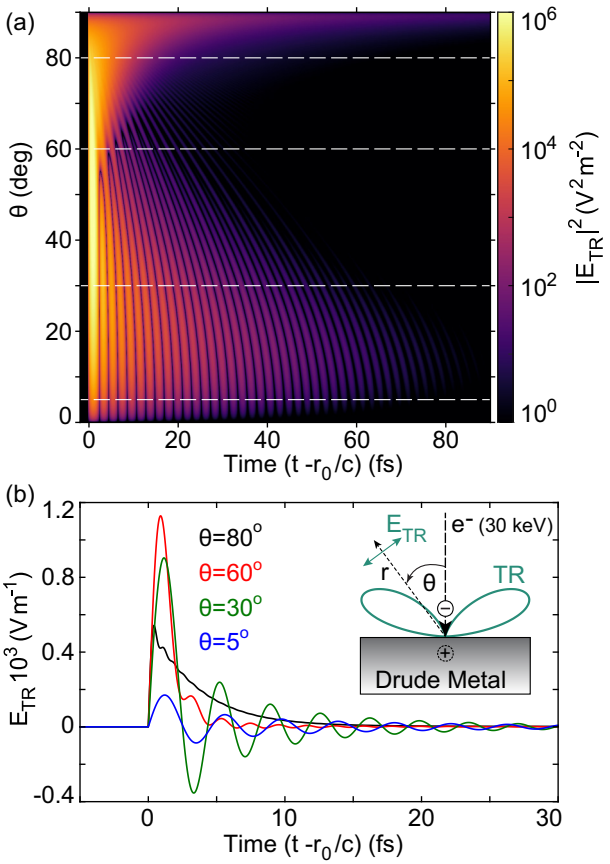

FIG. 5. Electric field of transition radiation (TR) excited by a 30 keV electron, propagating away from the same Drude metal as in Figs. 3 and 4, as a function of time. (a) The TR electric-field intensity, shown on a logarithmic scale, as a function of the emission angle θ and of the normalized time $T = t - r_0/c$, with $r_0 = \sqrt{2}$ μm the position at which the field is calculated for each angle [see inset schematic in (b)]. (b) Comparison of the TR electric-field amplitude as a function of the normalized time for four different emission angles, corresponding to the dashed lines in (a). The inset depicts a schematic of the TR excitation and emission process.

emission angles, we notice a variation in the maximum amplitude, with the smallest and largest angles exhibiting a lower intensity than those in between (by a factor ~2–5). This agrees with the expected dipolar emission pattern that also exhibits low intensity for small and large angles with a maximum in between. At small angles of emission, $\theta = 5°$ and 30°, we observe clear oscillations in time, which have a similar initial period before becoming out of phase after the second optical cycle. For higher emission angles, $\theta = 60°$ and 80°, the oscillations are strongly damped and the time evolution displays a single slow decay from the initial amplitude maximum.

In order to gain insight into this strong angle-dependent, short-lived behavior, we calculate the TR electric field as a function of frequency. Figure 6(a) shows the TR intensity as a function of frequency and emission angle. The intensity is limited to certain sections of θ-ω space. For the Drude metal with $\hbar\omega_p = 1$ eV, the permittivity approaches unity above an energy of several eV, so the electron will not perceive a

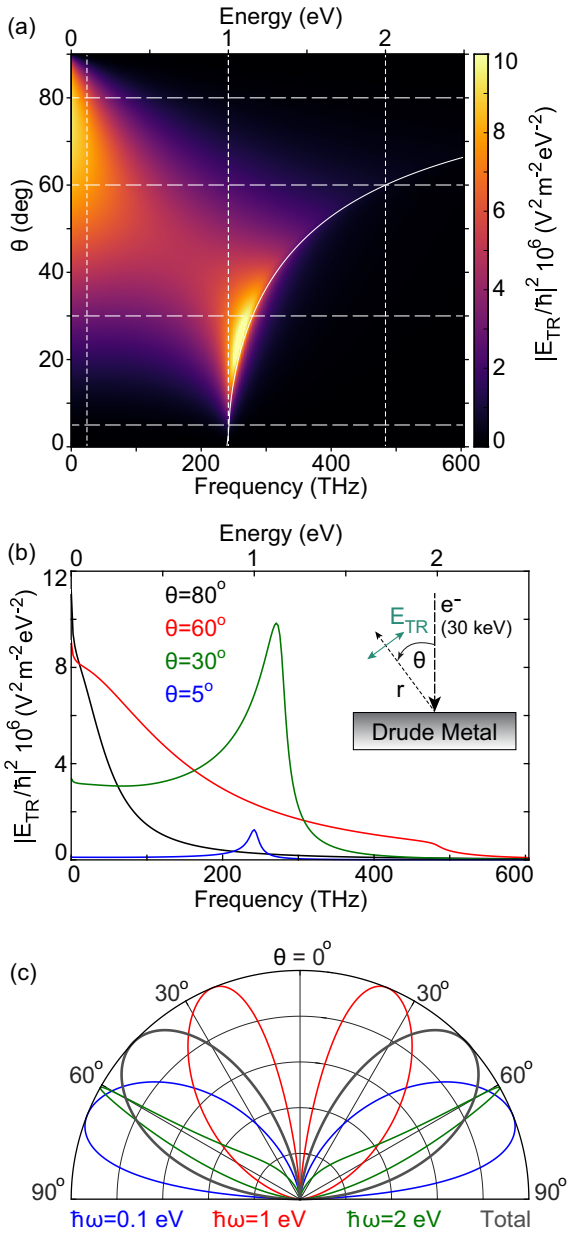

FIG. 6. Electric field of TR in the frequency domain, excited by a 30 keV electron impinging on the same Drude metal as in Figs. 3–5, evaluated at the same distance $r_0 = \sqrt{2}$ μm as in Fig. 5. (a) TR electric-field intensity as a function of emission angle θ and frequency/energy. The curved white line corresponds to $\theta = \arcsin(\sqrt{\epsilon_D})$. (b) Comparison of the TR electric-field spectra for different emission angles, denoted by the horizontal dashed lines in (a). The inset depicts a schematic of the TR excitation and emission geometry. (c) Normalized TR electric-field intensity as a function of emission angle, for the total integrated intensity (gray) and for different frequencies, denoted by the vertical dashed lines in (a).

transition in that energy range. The intensity is also depleted at the smallest and largest angles for most of the frequency range. Examining Eq. (23), we find that it contains a $\cos\theta$ term and a $\sin\theta$ term (due to Q), so $E_{\rm TR}$ is expected to go to 0 for angles close to 0 and $\pi/2$. Physically, these angles correspond to either very small Q or q_{zj}, indicating that the light modes are more delocalized (in space) and the coupling between the electrons and the impact region is smaller, leading to lower TR intensity.

At low frequencies and large angles (grazing to the surface), there is a broad and intense feature that occurs when the real and imaginary parts of ϵ_2 reach very large magnitudes ($\epsilon_2 = \epsilon_D$ of the Drude metal). At small angles (close to the surface normal), there is a sharp, bright peak that starts at $\omega = \omega_p$ and then bends off to higher frequencies and larger angles before disappearing around $\theta = 40°$. This feature occurs when $|\epsilon_D|$ displays a sharp kink and can be a result of an accumulation effect comparable to van Hove singularities [40,41]. The kink in $|\epsilon_D|$ bears resemblance to divergences in the density of states that lead to anomalies in optical absorption spectra. An additional explanation, described by Ferrell [42] and Stern [43] for metal foils, is that the incoming electron drives plasma oscillations of electrons at the surface, which radiate at the plasma frequency ω_p. This emission is only expected when $\mathrm{Im}\{\epsilon\}$ is much smaller than 1, which is the case here. In the Supplemental Material [31], we confirm that the effect indeed disappears for increasing loss.

We attribute the sudden depletion of the TR intensity of this feature for $\omega > \omega_p$ to the coupling strength between the electron and the material becoming focused in the forward direction, into the metal. The dispersion relation of the light inside the metal is given by $q = k\sqrt{\epsilon_D}$, while the parallel wave vector of the emitted radiation is $Q \leqslant q$. The boundary for coupling the energy into the metal instead of the far field of the upper hemisphere should thus be determined by $\sin\theta = Q/k = \sqrt{\epsilon_D}$, so $\theta = \arcsin(\sqrt{\epsilon_D})$. We find excellent agreement with the data, as confirmed by the curved solid white line in Fig. 6(a), as well as later on in Fig. 7 and in Fig. S5 of the Supplemental Material [31]. This explanation is consistent with the behavior of the μ_1 term [Eq. (9)] that appears in Eq. (23): the first denominator $q^2 - k^2\epsilon_D$ goes to 0 for $q = k\sqrt{\epsilon_D}$, leading to the divergent behavior that we observe.

These results indicate that the frequency-dependent permittivity of the Drude metal leaves a strong imprint on the TR emission. We will study this dependence on permittivity in more detail in Fig. 7. Additionally, we study the effect of different material parameters and electron energies on the TR emission explicitly in both the time and frequency domains in Figs. S3–S5 of the Supplemental Material [31].

While we present extensive results for a Drude metal with a characteristic bulk plasmon energy of 1 eV, the duration of the emitted wave packets of both SPPs and TR depends on η and ω_p. For a constant ratio between these quantities the pulse duration will be inversely proportional to ω_p, so that it becomes ∼15 times shorter for a prototypical Drude metal such as aluminum for example.

In Fig. 6(b), we examine the corresponding spectra for the same angles as shown in Fig. 5(b) (denoted by the horizontal white dashed lines). For $\theta = 5°$, we note a low intensity but a clear peak in the spectrum at the plasma frequency ω_p. For $\theta = 30°$, the spectrum is still dominated by this peak that has moved to slightly higher frequencies, but there is a noticeable increase at lower frequencies as well. We can now say that the oscillations in time from Fig. 5 for small angles correspond roughly to the plasma frequency. For larger angles, the frequency of oscillations increases. For $\theta = 60°$, a broad, decreasing spectral band is observed up to ∼2 eV (∼484 THz).

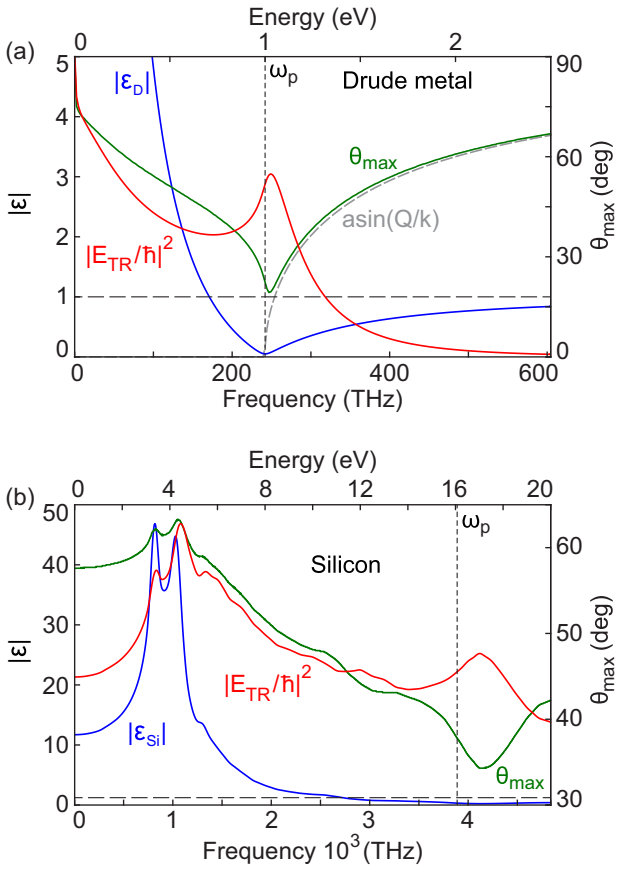

FIG. 7. Dependence of TR on the material permittivity ϵ. (a) Absolute value of the permittivity of the Drude metal ($\hbar\omega_p = 1$ eV and $\hbar\eta = 0.05$ eV), as a function of frequency/energy (in blue) compared to the normalized total TR electric-field intensity (integrated over all angles, in red) and the angle of maximum emission intensity $\theta_{\max}$ (in green). The TR intensity spectrum is normalized to the same maximum as $|\epsilon|$, the vertical dashed line denotes the plasma frequency, and the horizontal dashed line indicates $|\epsilon| = 1$. The gray dashed line corresponds to $\theta = \arcsin(Q/k) \sim \arcsin(\sqrt{\epsilon})$. (b) Same as for (a), but now for silicon, with a permittivity that displays typical features of a dielectric but also contains a metallic region.

At $\theta = 80°$, a narrower spectral band is distinguished, falling off well below 1 eV. These data correspond to the time evolution that is observed at large angles, which does not exhibit clear oscillations but instead a strongly decaying signal.

Examining the frequency extent of the spectra more closely, they are most confined for the largest and smallest angles [Figs. 6(a) and 6(b)], where the fields are more delocalized. Correspondingly, the TR is more spread out in time. For angles around $\theta = 50$–$70°$, the fields extend over a much wider range of frequencies and are very localized in time, corresponding to stronger coupling between the electrons and the impact region. Combining the fields over all angles and determining the far-field component, as described in Eq. (24), allows one to calculate the emission intensity that can be measured experimentally. This approach has shown excellent agreement with multiple experiments on a variety of materials, including metals and semiconductors [44–46].

In addition to studying the spectra for given angles, we can determine the angular profile at different frequencies. This is experimentally accessible, for example, by using angle-resolved detection in combination with spectral filters. As for spectral measurements, good agreement with theory has been found for a variety of materials [46,47]. Figure 6(c) presents the normalized intensity as a function of θ for the frequencies corresponding to the vertical white dashed lines in Fig. 6(a), as well as the total intensity summed over all frequencies. We clearly observe the characteristic dipolar lobes, which vary in orientation and width for different frequencies. As expected, there are broader lobes at grazing angles for low frequencies and narrower lobes close to the surface normal at $\omega = \omega_p$. For higher frequencies, the distribution moves back to higher angles and becomes sharper.

Figure 7 examines the relation between TR emission and material permittivity by comparing the absolute value of ϵ to the total intensity (summed over all angles) and to the angle of maximum intensity $\theta_{\max}$, as a function of frequency/energy. The incoming medium is vacuum. We first study the Drude metal with $\hbar\omega_p = 1$ eV and $\hbar\eta = 0.05$ eV for a 30 keV electron [Fig. 7(a)]. For low frequencies, $|\epsilon_D|$ and the total intensity exhibit the same decreasing trend when approaching ω_p; the two then show opposite behavior in the frequency range where $|\epsilon_D| < 1$. $\theta_{\max}$, meanwhile, displays the same trend as ϵ_D across the whole frequency range, decreasing and increasing in lockstep. We examine the angle $\theta = \arcsin(\sqrt{\epsilon_D})$ for frequencies $\omega > \omega_p$, indicated by the gray dashed line. As discussed above, this should indicate the boundary between regions where the radiation is coupled in the backward (upper hemisphere) or forward (into the metal) directions. The resulting angle exhibits excellent agreement with $\theta_{\max}$, indicating that the sudden depletion of TR can indeed be attributed to coupling into the metal. This is dependent on the specific material permittivity; we confirm that there is good agreement for different parameters in Fig. S5 of the Supplemental Material [31].

In order to further explore these trends, we examine the same variables for silicon in Fig. 7(b), again using a 30 keV electron. In the $\hbar\omega = 0$–20 eV range, the permittivity ϵ_{Si} of silicon displays a strong double peak around 4 eV (~967 THz) and $\mathrm{Re}\{\epsilon_{\mathrm{Si}}\} < 0$ from 4 to 16 eV (~967–3869 THz). $|\epsilon_{\mathrm{Si}}|$ and $\theta_{\max}$ follow the same trend over the entire frequency range, while the total TR intensity again exhibits the same trend as $|\epsilon_{\mathrm{Si}}|$ for frequencies where $|\epsilon_{\mathrm{Si}}| > 1$ and an opposite trend for frequencies where $|\epsilon_{\mathrm{Si}}| < 1$. As for the Drude model, the minimum of $|\epsilon_{\mathrm{Si}}|$ and $\theta_{\max}$ corresponds to a peak in the total intensity.

Determining a direct relation between ϵ and all aspects of the TR emission is difficult because ϵ appears multiple times in the equations, but it is possible to get an intuitive understanding of the behavior. Looking back at the definition of TR, it is essentially a "reflected" field induced by the approaching electron that has to adapt to its new electromagnetic environment. The term μ_j from the equations even bears some resemblance to the Fresnel equations. Just as for reflection of light, one can understand that the higher the contrast between the two media, the more the field of the electron will have to "shake off" components and induce a strong response [48]. The ratio between the permittivities of the two materials can go both ways, however. What we observe in Fig. 7 is that for

both $|\epsilon| \gg 1$ and $|\epsilon| \ll 1$, the TR intensity is high due to the large contrast from 1. The angle of maximum emission θ_{max} consistently follows the same trend as $|\epsilon|$. In Figs. S6 and S7 of the Supplemental Material [31], we study this in more detail.

VI. CONCLUSIONS

We have determined that transition radiation and surface plasmon polaritons excited by swift electrons are composed of ultrashort, femtosecond time-scale wave packets. We have studied the time, space, and frequency dependence of the electric fields induced by the electron, both in vacuum and when traversing a metallic or dielectric surface, providing intuitive physical insight into these ultrafast processes. The external field of the swift electron in vacuum comprises a single oscillation, similar to a single optical cycle, and thus represents an ultrabroadband optical excitation spectrum. In vacuum, the fields evanescently decay away from the electron trajectory and cannot directly couple to radiation. When impinging on a polarizable material, however, the electron induces fields at the surface that can radiate out to the far field.

We first studied the surface plasmon polaritons propagating along the surface of a Drude metal, finding that the plasmon wave packets are several-hundred femtoseconds in duration (depending on the material parameters). The SPPs decay rapidly and redshift in frequency as they propagate away from the point of excitation. This redshift is due to the fact that high-frequency components close to the plasmon resonance are strongly damped.

We have also examined transition radiation, the far-field emission which occurs when a charged particle traverses the interface between two different media. Using the Drude metal as an example, we find that TR wave packets are strongly dependent on the emission angle and ultrashort in duration, lasting only a few tens of femtoseconds (again depending on the material parameters). The TR intensity and emission-angle dependence is correlated with well-defined trends in the permittivity of the material. Given the frequency dependence of ϵ for a certain dielectric, the TR emission can be qualitatively predicted.

The theoretical insights and predictions presented here further our knowledge and understanding of electron-light-matter interactions at the nanoscale and can be applied to study fundamental physical processes occurring at the femtosecond time scale.

ACKNOWLEDGMENTS

We would like to acknowledge Toon Coenen, Mark W. Knight, Iván Silveiro, José R. M. Saavedra, and Sophie Meuret for useful discussions. This work is part of the research program of the "Stichting voor Fundamenteel Onderzoek der Materie (FOM)," which is financially supported by the "Nederlandse Organisatie voor Wetenschappelijk Onderzoek (NWO)." This work is part of NanoNextNL, a nanotechnology program funded by the Dutch Ministry of Economic Affairs and is also supported by the European Research Council (ERC). F.J.G.-A. acknowledges support from the Spanish MINECO (Grants No. MAT2014-59096-P and No. SEV2015-0522).

[1] F. J. García de Abajo, Rev. Mod. Phys. **82**, 209 (2010).
[2] G. Adamo, K. F. MacDonald, N. I. Zheludev, Y. H. Fu, C. M. Wang, D. P. Tsai, and F. J. García de Abajo, Phys. Rev. Lett. **103**, 113901 (2009).
[3] K. Kimoto, T. Asaka, T. Nagai, M. Saito, Y. Matsui, and K. Ishizuka, Nature (London) **450**, 702 (2007).
[4] R. Sapienza, T. Coenen, J. Renger, M. Kuttge, N. F. van Hulst, and A. Polman, Nat. Mater. **11**, 781 (2012).
[5] M. V. Bashevoy, F. Jonsson, K. F. MacDonald, Y. Chen, and N. I. Zheludev, Opt. Express **15**, 11313 (2007).
[6] J. A. Scholl, A. L. Koh, and J. A. Dionne, Nature (London) **483**, 421 (2012).
[7] T. Coenen, F. Bernal Arango, A. F. Koenderink, and A. Polman, Nat. Commun. **5**, 3250 (2014).
[8] F. J. García de Abajo and M. Kociak, Phys. Rev. Lett. **100**, 106804 (2008).
[9] U. Hohenester, H. Ditlbacher, and J. R. Krenn, Phys. Rev. Lett. **103**, 106801 (2009).
[10] W. Cai, R. Sainidou, J. Xu, A. Polman, and F. J. García de Abajo, Nano Lett. **9**, 1176 (2009).
[11] A. Asenjo-Garcia and F. J. García de Abajo, New J. Phys. **15**, 103021 (2013).
[12] A. Hörl, A. Trügler, and U. Hohenester, Phys. Rev. Lett. **111**, 076801 (2013).
[13] A. Losquin and M. Kociak, ACS Photon. **2**, 1619 (2015).
[14] A. Feist, K. E. Echternkamp, J. Schauss, S. V. Yalunin, S. Schäfer, and C. Ropers, Nature (London) **521**, 200 (2015).
[15] L. Piazza, T. T. A. Lummen, E. Quinonez, Y. Murooka, B. W. Reed, B. Barwick, and F. Carbone, Nat. Commun. **6**, 6407 (2015).
[16] C. Matyssek, J. Niegemann, W. Hergert, and K. Busch, Phot. Nano. Fund. Appl. **9**, 367 (2011).
[17] K. Busch, M. König, and J. Niegemann, Laser Photon. Rev. **5**, 773 (2011).
[18] M. Abramowitz and I. A. Stegun, *Handbook of Mathematical Functions* (Dover Publications, New York, 1964), Vol. 55.
[19] J. D. Jackson, *Classical Electrodynamics*, 3rd ed. (Wiley, New York, 1999).
[20] M. O. Scully and M. S. Zubairy, *Quantum Optics*, 1st ed. (Cambridge University Press, Cambridge, 1997).
[21] J.-J. Greffet, M. Laroche, and F. Marquier, Phys. Rev. Lett. **105**, 117701 (2010).
[22] F. J. García de Abajo, A. Rivacoba, N. Zabala, and N. Yamamoto, Phys. Rev. B **69**, 155420 (2004).
[23] C. J. Powell and J. B. Swan, Phys. Rev. **115**, 869 (1959).
[24] Y.-Y. Teng and E. A. Stern, Phys. Rev. Lett. **19**, 511 (1967).
[25] D. Heitmann, J. Phys. C **10**, 397 (1977).
[26] M. V. Bashevoy, F. Jonsson, A. V. Krasavin, N. I. Zheludev, Y. Chen, and M. I. Stockman, Nano Lett. **6**, 1113 (2006).

[27] M. Kuttge, E. J. R. Vesseur, A. F. Koenderink, H. J. Lezec, H. A. Atwater, F. J. García de Abajo, and A. Polman, Phys. Rev. B **79**, 113405 (2009).
[28] J. van Wijngaarden, E. Verhagen, A. Polman, C. Ross, H. J. Lezec, and H. A. Atwater, Appl. Phys. Lett. **88**, 221111 (2006).
[29] G. W. Ford and W. H. Weber, Phys. Rep. **113**, 195 (1984).
[30] A. Archambault, T. V. Teperik, F. Marquier, and J.-J. Greffet, Phys. Rev. B **79**, 195414 (2009).
[31] See Supplemental Material at http://link.aps.org/supplemental/10.1103/PhysRevB.94.155412 doi for the full time and frequency dependencies as a function of distance for SPPs and TR, comparing different material and electron parameters, as well as a more detailed analysis of the dependence of TR on material permittivity.
[32] V. L. Ginzburg and I. M. Frank, J. Phys. (USSR) **9**, 353 (1945).
[33] V. L. Ginzburg, Phys. Usp. **39**, 973 (1996).
[34] P. Goldsmith and J. Jelley, Philos. Mag. **4**, 836 (1959).
[35] M. L. Ter-Mikaelian, *High-Energy Electromagnetic Processes in Condensed Media*, Vol. 29 (Wiley, New York, 1972).
[36] E. Kröger, Z. Phys. **216**, 115 (1968).
[37] E. M. Purcell, *Electricity and Magnetism* (McGraw-Hill, New York, 1983).
[38] B. M. Bolotovskii and A. V. Serov, Nucl. Instrum. Methods Phys. Res., Sect. B **145**, 31 (1998).
[39] A. Serov and B. M. Bolotovskii, J. Expt. Theor. Phys. **104**, 866 (2007).
[40] L. Van Hove, Phys. Rev. **89**, 1189 (1953).
[41] F. Bassani and G. P. Parravicini, *Electronic States and Optical Transitions in Solids* (Pergamon, New York, 1975).
[42] R. A. Ferrell, Phys. Rev. **111**, 1214 (1958).
[43] E. A. Stern, Phys. Rev. Lett. **8**, 7 (1962).
[44] N. Yamamoto, K. Araya, A. Toda, and H. Sugiyama, Surf. Interface Anal. **31**, 79 (2001).
[45] N. Yamamoto, H. Sugiyama, and A. Toda, Proc. R. Soc. A **452**, 2279 (1996).
[46] B. J. M. Brenny, T. Coenen, and A. Polman, J. Appl. Phys. **115**, 244307 (2014).
[47] T. Coenen, E. J. R. Vesseur, and A. Polman, Appl. Phys. Lett. **99**, 143103 (2011).
[48] N. Yamamoto, A. Toda, and K. Araya, J. Electron Microscop. **45**, 64 (1996).

Supplemental Material: Femtosecond plasmon and photon wave packets excited by a high-energy electron on a metal or dielectric surface

Benjamin J. M. Brenny,[1] Albert Polman,[1,*] and F. J. García de Abajo[2,3,†]

[1]*Center for Nanophotonics, FOM Institute AMOLF, Science Park 104, 1098 XG Amsterdam, The Netherlands*

[2]*ICFO-Institut de Ciencies Fotoniques, 08860 Castelldefels (Barcelona), Spain*

[3]*ICREA-Institució Catalana de Recerca i Estudis Avancats, Passeig Lluís Companys, 23, 08010 Barcelona, Spain*

I. FULL TIME, FREQUENCY AND MATERIAL DEPENDENCE OF SPPS

In Section **IV** of the main text, we discuss how a fast electron impinging on a metal surface can excite surface plasmon polaritons (SPPs). These propagate along the surface as femtosecond-scale wave packets, decaying in intensity with gradually decreasing frequencies as they travel further away from the excitation position. We have shown the time evolution and spectral behavior of the SPP electric fields for a selection of distances in Figure 3.

In order to give a more complete overview of the traveling waves, we display a full range of distances here in Figure S1. We first examine the intensity of the E_z component as a function of time t (up to 200 fs) and radial distance R (up to 60 μm), in Figure S1(a). We multiply the intensity by the radial distance R to compensate for its $1/R$ dependence. The color scale is saturated in order to view the features over the entire range. Since the SPP travels as a wave packet over the surface, it displays oscillations both as a function of time and of the distance R, moving at a speed given by the slope in the figure. We observe clear waves oriented diagonally, with slopes corresponding to velocities close to but slower than the speed of light (white dashed line). Very close to the origin, the oscillations in time are much faster and the slopes are smaller (corresponding to lower velocities) than for further distances. This is in agreement with the expected behavior of the SPPs given their dispersion, as discussed in the description of Figure 3.

The inset of Figure S1(a) exhibits a snapshot of the SPP E_z intensity (multiplied by R) at t=50 fs, as a function of R and z. We observe, as can be expected, that the field intensity decays for increasing R and $|z|$ and that there is more intensity at the incoming vacuum side ($z < 0$). The period of the oscillations also increases with R, in accordance with the damping that leads to smaller Q_{SPP} (longer wavelengths) as the SPPs propagate further away from the point of excitation.

Figure S1(b) displays the corresponding information in the frequency domain, with the intensity of the E_z component (multiplied by R) plotted as a function of frequency and the same radial distance range. For small R we find that the spectrum extends up to the plasmon resonance $\omega_{\mathrm{SPP}} \sim$0.7 eV (see Figure 3(d)). For increasing distance, the spectrum gradually shifts to lower frequencies, peaking near ∼0.25 eV for R=60 μm.

To gain a better understanding of the SPP dependence on material properties and the energy of the exciting electron, we compare the time and frequency evolution for different

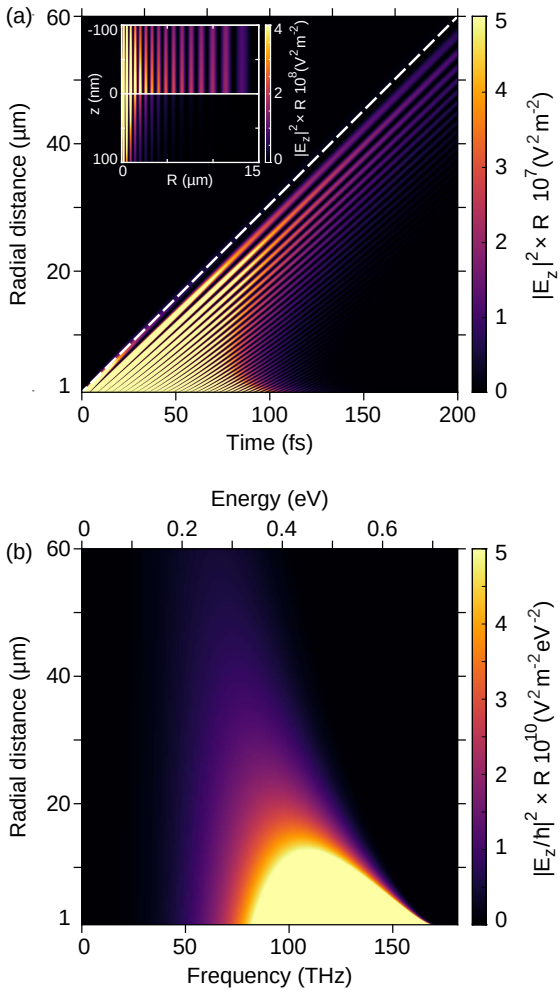

FIG. S1. Electric field E_z of surface plasmon polaritons (SPPs) excited by a 30 keV electron, propagating over the surface of a Drude metal ($\hbar\omega_p$=1 eV and $\hbar\eta$=0.05 eV), calculated at a distance z=−10 nm from the surface, as in Figure 3. (a) Intensity of the SPP E_z field component multiplied by the radial distance R, as a function of time t and radial distance R away from the electron trajectory. The color scale is saturated in order to distinguish the oscillations of the SPP wave packet over the entire range, the maximum intensity (at the origin) is 2.4×10^{11} (V^2 m^{-2}). The diagonal white dashed line represents the light cone. The inset shows a 2D R–z snapshot at t=50 fs of the E_z intensity multiplied by R. (b) The corresponding intensity of the SPP E_z field component in the frequency domain multiplied by the radial distance R, as a function of the frequency and radial distance R. We again saturate the color scale to distinguish the redshift of the frequencies over the entire range, the maximum intensity (at the origin) is 5.5×10^{14} (V^2 m^{-2}).

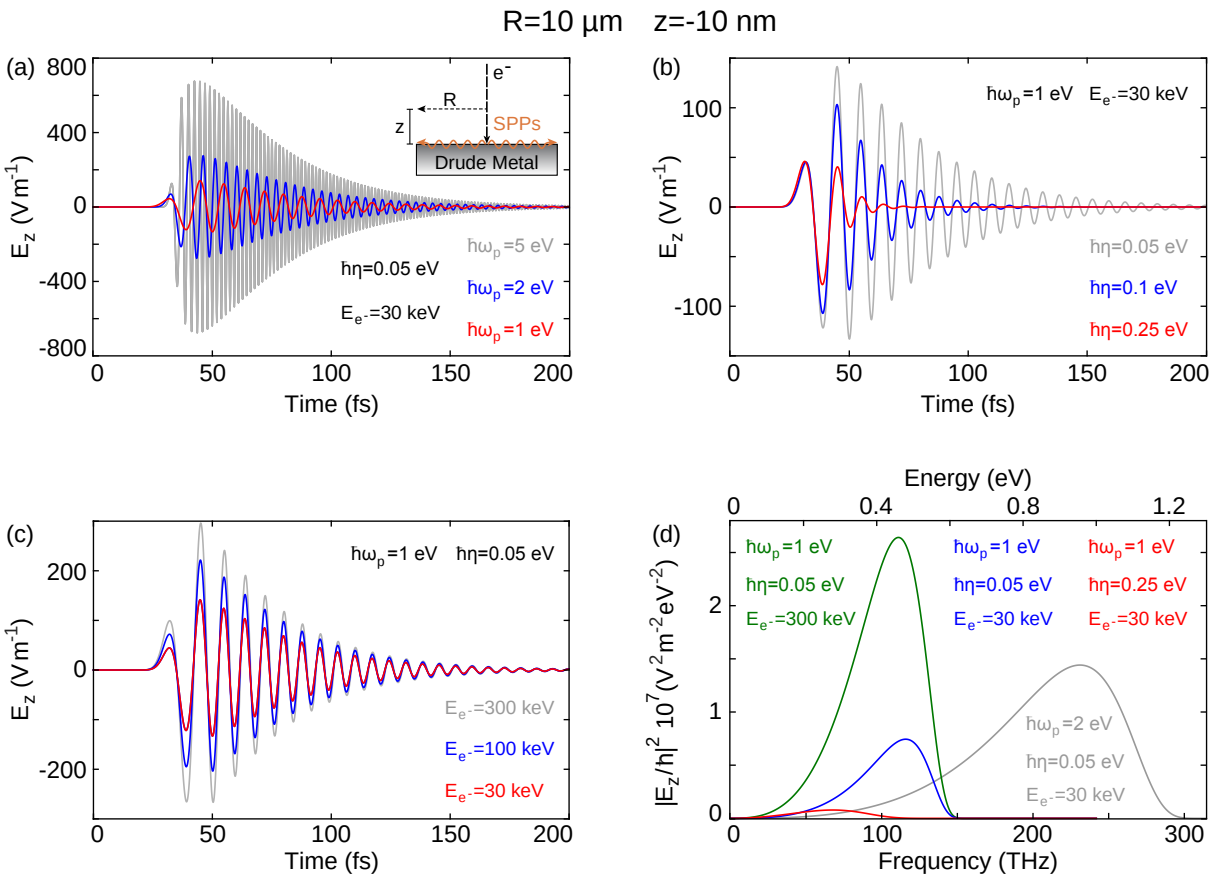

FIG. S2. Comparison of the SPP electric field for different Drude metals and electron energies, all for the same radial distance R=10 μm and fixed height z=−10 nm. (a) Varying the plasma frequency for fixed loss ($\hbar\eta$=0.05 eV) and electron energy (E_{e^-}=30 keV), showing the time dependence of the E_z SPP amplitude as a function of time t for $\hbar\omega_p$=1 eV (in red), $\hbar\omega_p$=2 eV (in blue), and $\hbar\omega_p$=5 eV (in gray). The inset in (a) shows a simplified schematic of the SPP excitation and emission process. (b) E_z SPP amplitude with fixed $\hbar\omega_p$=1 eV and E_{e^-}=30 keV, for $\hbar\eta$=0.25 eV (in red), $\hbar\eta$=0.1 eV (in blue), and $\hbar\eta$=0.05 eV (in gray). (c) E_z SPP amplitude with fixed $\hbar\omega_p$=1 eV and $\hbar\eta$=0.25 eV, for E_{e^-}=30 keV (in red), E_{e^-}=100 keV (in blue), and E_{e^-}=300 keV (in gray). (d) E_z SPP intensity as a function of frequency, for the parameters used in main text ($\hbar\omega_p$=1 eV, $\hbar\eta$=0.05 eV, and E_{e^-}=30 keV, in blue); a more energetic exciting electron ($\hbar\omega_p$=1 eV, $\hbar\eta$=0.05 eV, and E_{e^-}=300 keV, in green); a Drude metal with more losses ($\hbar\omega_p$=1 eV, $\hbar\eta$=0.25 eV, and E_{e^-}=30 keV, in red); a Drude metal with a higher plasma frequency ($\hbar\omega_p$=2 eV, $\hbar\eta$=0.05 eV, and E_{e^-}=30 keV, in gray).

combinations of ω_p, η and the electron energy $\mathrm{E_{e^-}}$ in Figure S2. The calculations use the same radial distance R=10 µm and height z=−10 nm. We examine the time evolution of the E_z SPP amplitude for increasing ω_p in Figure S2(a), increasing η in Figure S2(b), and higher $\mathrm{E_{e^-}}$ in Figure S2(c). Figure S2(d) compares the E_z SPP intensity as a function of frequency for a subset of these different parameters.

Studying the decay duration of the SPP wave packets in the time domain, it appears that only changing the plasma frequency and electron energy does not have a noticeable effect. This is confirmed by comparing the normalized amplitudes (not shown here). The initial onset of the wave packet does change slightly for increasing ω_p, starting later for higher frequencies, but the time of maximum amplitude and the subsequent decay do not differ. Increasing the damping η (Figure S2(b)), however, noticeably shortens the wave packet duration and also decreases the maximum field amplitude. Examining the frequency response in Figure S2(d) we find a correspondingly lower intensity, combined with a redshift. This is to be expected, since η governs the absorption or damping in the Drude metal. In a more general way, however, all time scales in the system are determined by ω_p. For a fixed ratio of η and ω_p, the wave packet duration should be inversely proportional to ω_p. In this way a prototypical Drude metal such as aluminum ($\hbar\omega_\mathrm{p} = 15$ eV, $\omega_\mathrm{p}/\eta \sim 30$) will exhibit SPP and TR wave packets that have a much shorter duration than the Drude metal used in the main text ($\hbar\omega_\mathrm{p} = 1$ eV, $\omega_\mathrm{p}/\eta = 20$).

Increasing the plasma frequency leads to a clear increase in the field amplitude (Figure S2(a)) and corresponding intensity in the spectra (Figure S2(d)). A higher number of conduction electrons are involved for higher plasma frequencies ($\omega_\mathrm{p}^2 \propto N_e$) and according to the *f*-sum rule, light extinction (the sum of absorption and scattering) generally scales with N_e[1–3]. The interaction strength and SPP generation thus increases with plasma frequency.

Increasing the electron energy (Figure S2(c)) only has a significant effect on the field amplitude, which grows by roughly a factor of two for a ten times higher energy. The period of the oscillations also slightly increases. Both of these differences are also observed in the frequency domain (Figure S2(d)), with a higher intensity and small redshift for the 300 keV electron compared to 30 keV. The field strength enhancement results from the fact that at higher velocities, the fields extend further (as determined by the Bohr cutoff $v\gamma_\epsilon/\omega$). This increases the volume of polarized material, which leads to a stronger induced field and a higher generation rate of SPPs. The very slight difference in the time evolution and

corresponding frequency could be related to a different degree of retardation. Overall, we find that changing the material properties has a much stronger effect on the SPP behavior than varying the energy of the incident electron. We will now examine if the same holds true for TR.

II. FULL COMPARISON OF TR FOR DIFFERENT MATERIAL/ELECTRON PARAMETERS

Section **V** of the main text describes how a fast electron impinging on a second medium (a Drude metal) will generate transition radiation (TR) as it transits through the interface and the electric fields change to adapt to their new environment. TR takes the form of ultrashort wave packets a few tens of femtoseconds in duration, that are highly dependent on the emission angles and material permittivity. Here in Figures S3, S4 and S5 we study the effect of different material properties and electron energy on the TR emission behavior.

In the main text, we have examined the time, angle and frequency dependence of TR emission for one specific instance ($\hbar\omega_p$=1 eV and $\hbar\eta$=0.05 eV, E_{e^-}=30 keV). Figure S3 compares the time evolution and spectra for those parameters, at θ=5° and θ=60°, to three additional cases. We either change the electron energy to 300 keV, or increase the loss in the Drude metal tenfold to $\hbar\eta$=0.5 eV, or double the plasma frequency to $\hbar\omega_p$=2 eV. For completeness, Figures S4 and S5 display the field intensity in the time and frequency domains, for all emission angles. First examining the time-dependent behavior in Figures S3(a,b), we find that for increased damping, the field amplitude oscillations die out more rapidly, while for the higher plasma frequency the field amplitude is increased and oscillates about twice as fast. For the higher electron energy, we observe an increase in amplitude, accompanied with a slight change in the frequency of the oscillations. The increase in field strength can be intuitively understood for the same reason as for the SPPs: the electron fields extend further away, polarizing a larger volume of material. The wave packet decay duration and the frequency of oscillations are also directly related to η and ω_p respectively, as we saw for the SPPs in Figure S2. Similarly, the overall pulse duration should scale inversely with ω_p (given a constant ratio between ω_p and η).

Figures S3(c,d) show the corresponding data for θ=5° and 60° in the frequency domain. For the increased η the spectra are less intense, especially for θ=5°, where the peak close to

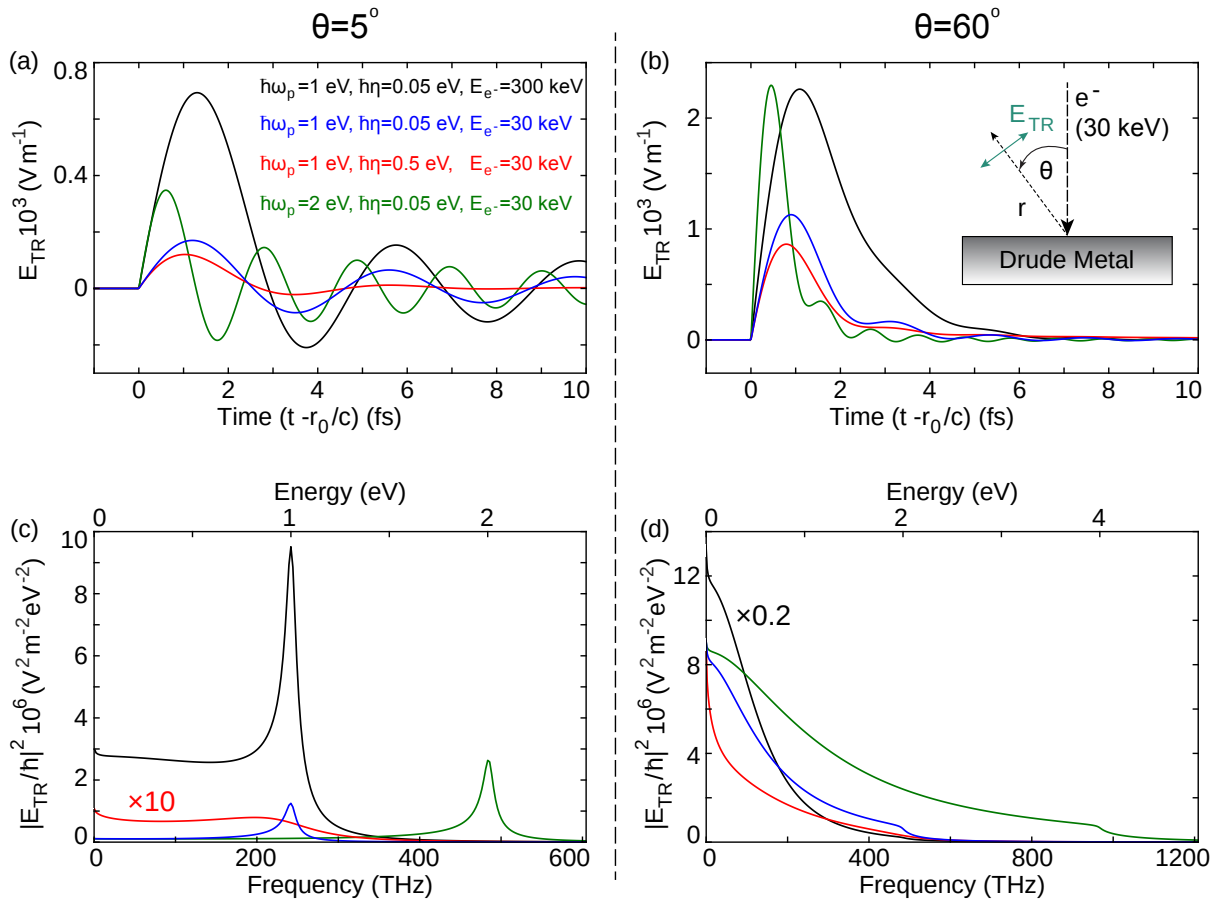

FIG. S3. Comparison of the TR electric field for different Drude metals and electron energies. We compare the parameters used in the main text ($\hbar\omega_p$=1 eV and $\hbar\eta$=0.05 eV, E_{e^-}=30 keV, in blue) to a more energetic exciting electron ($\hbar\omega_p$=1 eV and $\hbar\eta$=0.05 eV, E_{e^-}=300 keV, in black), a Drude metal with more losses ($\hbar\omega_p$=1 eV and $\hbar\eta$=0.5 eV, E_{e^-}=30 keV, in red) and a Drude metal with a higher plasma frequency ($\hbar\omega_p$=2 eV and $\hbar\eta$=0.05 eV, E_{e^-}=30 keV, in green). We show the time dependence of the TR electric field amplitude as a function of normalized time (T=$t - r_0/c$) for an emission angle of θ=5° (a) and θ=60° (b). We also show the TR electric field intensity in the frequency domain, as a function of frequency for these same angles (c,d). The red spectrum in (c) has been multiplied by a factor of 10, while the black spectrum in (d) has been multiplied by a factor 0.2. The inset in (b) shows a simplified schematic of the TR excitation and emission process.

ω=ω_p has broadened and red shifted slightly. For $\hbar\omega_p$=2 eV the peak at θ=5° has increased in intensity and blue shifted to twice the frequency, as expected. The same trend holds for

θ=60°. As for the SPPs, the increase in intensity can be related to the higher conduction electron density and the *f*-sum rule. The calculation with 300 keV electron energy shows the same general spectral behavior as for 30 keV, with a higher intensity and a stronger contribution from low frequencies, for both angles. This agrees well with the time evolution, where we observe that the wave packet for 300 keV lags very slightly and oscillates a little slower than for 30 keV (by ∼0.2 fs). Overall, we find that the dependence of TR on material parameters and electron energy is very similar to that of the SPPs.

Figure S4 displays the TR electric field intensity as a function of the emission angle θ and the normalized time $T{=}t - r_0/c$. As expected, a higher loss factor η leads to TR oscillations that are much more damped, over all emission angles. A higher plasma frequency leads to faster oscillations, except for the most grazing angles where the emission is still critically damped. The faster electron with 300 keV energy mostly leads to an increase in intensity, relatively more noticeable for the higher emission angles.

Figure S5 shows the corresponding information in the frequency domain, with panels (a–d) corresponding to the same parameters as in Figure S4. The calculation for higher loss displays a much weaker overall intensity and a disappearance of the feature at $\omega{=}\omega_\mathrm{p}$, explaining the absence of a well-defined peak for this case in Figure S3(c). For the higher electron energy (Figure S5(c)) the bright feature at low angles close to ω_p is well-preserved, but we notice a clear relative increase of the intensity at low frequencies, over a wide angular range. The doubled plasma frequency (Figure S5(d)) shows a shift of the sharp bright feature at low angles to the new plasma frequency, which is now relatively more intense than the feature at high angles and low frequencies. This change is quite opposite to that observed for the increased electron energy. We discussed in the main text that the TR emission should be depleted when the electron couples its energy into the material instead of radiation into the upper hemisphere. The angle determining this boundary, $\theta = \arcsin(\sqrt{\epsilon})$, is shown as a white dashed line in all four panels and exhibits excellent agreement with the trend of the TR intensity as it transitions between bright and dark regions for $\omega > \omega_\mathrm{p}$. Since we only use the real part of ϵ to determine this angle, we do not account for the strong damping in Figure S5(c), which causes the feature to disappear. This is in agreement with Stern[4], who predicts a peak in TR at the plasma frequency when the imaginary part of ϵ is much smaller than 1, which does not apply for the larger η used here. As for the SPPs, the material parameters have a stronger influence than the electron energy.

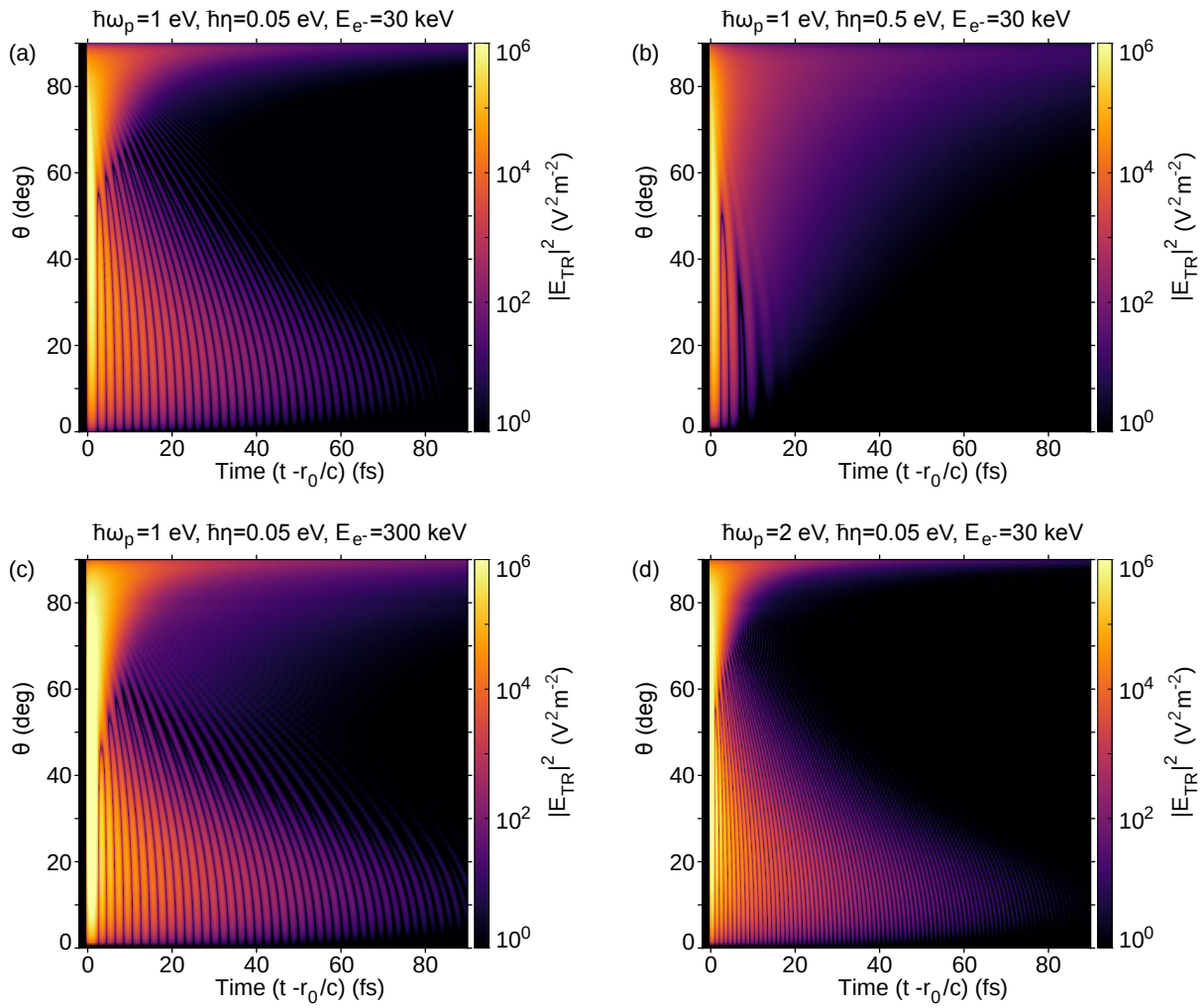

FIG. S4. Comparison of the full time evolution of the TR electric fields for the different Drude metals and electron energies from Figures S3. We show the TR electric field intensity on a logarithmic scale, as a function of normalized time (T=$t - r_0/c$) and emission angle θ. (a) TR intensity for $\hbar\omega_{\mathrm{p}}$=1 eV and $\hbar\eta$=0.05 eV, $\mathrm{E_{e^-}}$=30 keV. (b) A more lossy Drude metal, $\hbar\omega_{\mathrm{p}}$=1 eV and $\hbar\eta$=0.5 eV, $\mathrm{E_{e^-}}$=30 keV. (c) A more energetic exciting electron, $\hbar\omega_{\mathrm{p}}$=1 eV and $\hbar\eta$=0.05 eV, $\mathrm{E_{e^-}}$=300 keV. (d) A Drude metal with a higher plasma frequency, $\hbar\omega_{\mathrm{p}}$=2 eV and $\hbar\eta$=0.05 eV, $\mathrm{E_{e^-}}$=30 keV.

III. DEPENDENCE OF TR ON MATERIAL PERMITTIVITY

Figure 6 from Section **V** describes how the emission behavior of TR correlates with the permittivity of the medium onto which the electron impinges (now denoted as ϵ, the incoming medium always being vacuum). Here we study this relation in more detail. Figure S6 displays

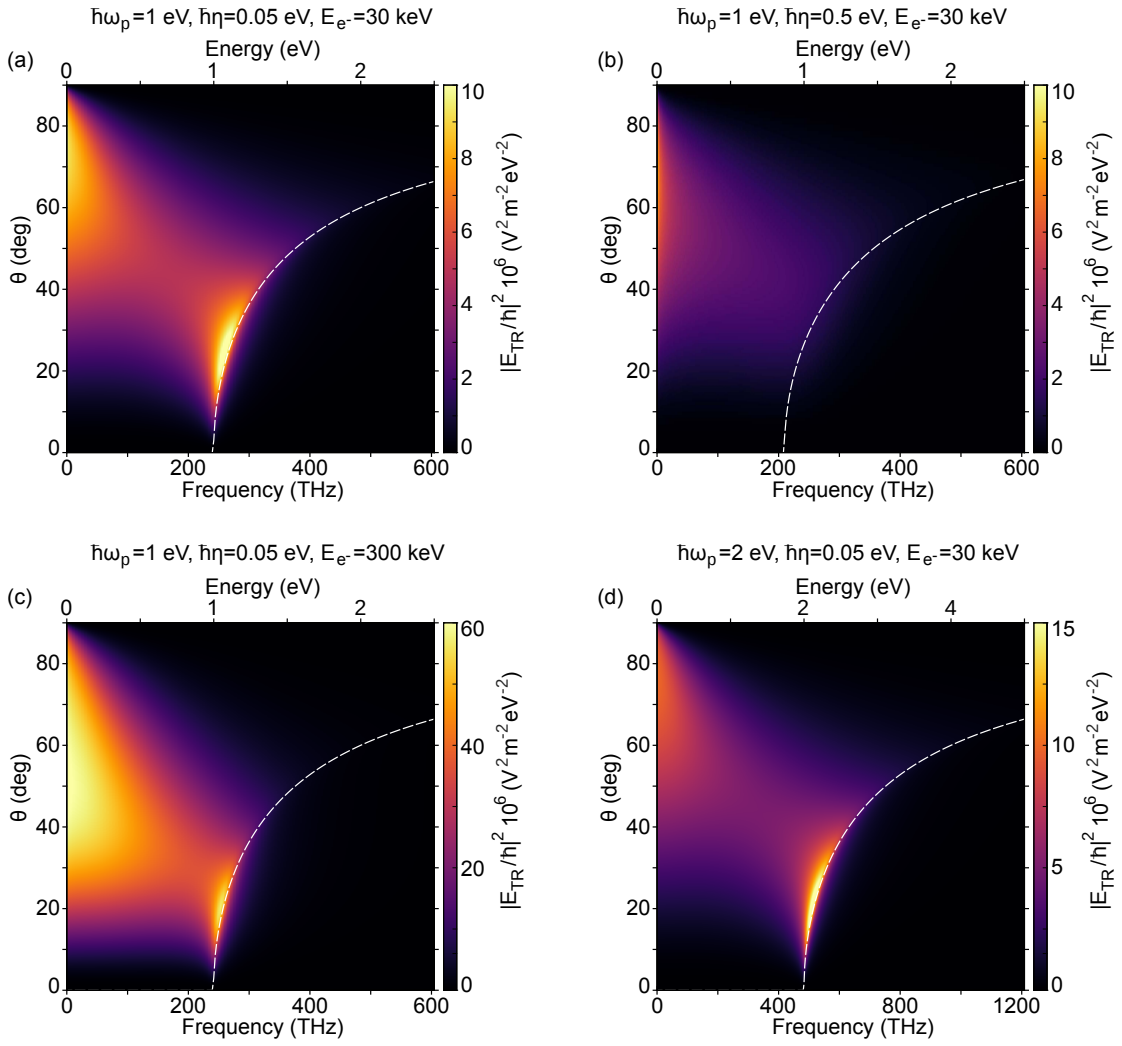

FIG. S5. Comparison of the full spectral behavior of the TR electric fields for the different Drude metals and electron energies from Figure S3. We show the TR electric field intensity as a function of frequency and emission angle θ. (a) TR intensity for $\hbar\omega_p$=1 eV and $\hbar\eta$=0.05 eV, E_{e^-}=30 keV. (b) A more lossy Drude metal, $\hbar\omega_p$=1 eV and $\hbar\eta$=0.5 eV, E_{e^-}=30 keV. (c) A more energetic exciting electron, $\hbar\omega_p$=1 eV and $\hbar\eta$=0.05 eV, E_{e^-}=300 keV. (d) A Drude metal with a higher plasma frequency, $\hbar\omega_p$=2 eV and $\hbar\eta$=0.05 eV, E_{e^-}=30 keV. The white dashed lines correspond to $\theta = \arcsin(Q/k) \sim \arcsin(\sqrt{\epsilon})$, with ϵ given by the Drude parameters. We note that (a) and (b) are shown on the same scale, but (c) and (d) have different scales.

the results for an artificial frequency-dependent ϵ with specific features, to determine the underlying principles behind the behavior observed in Figure 6.

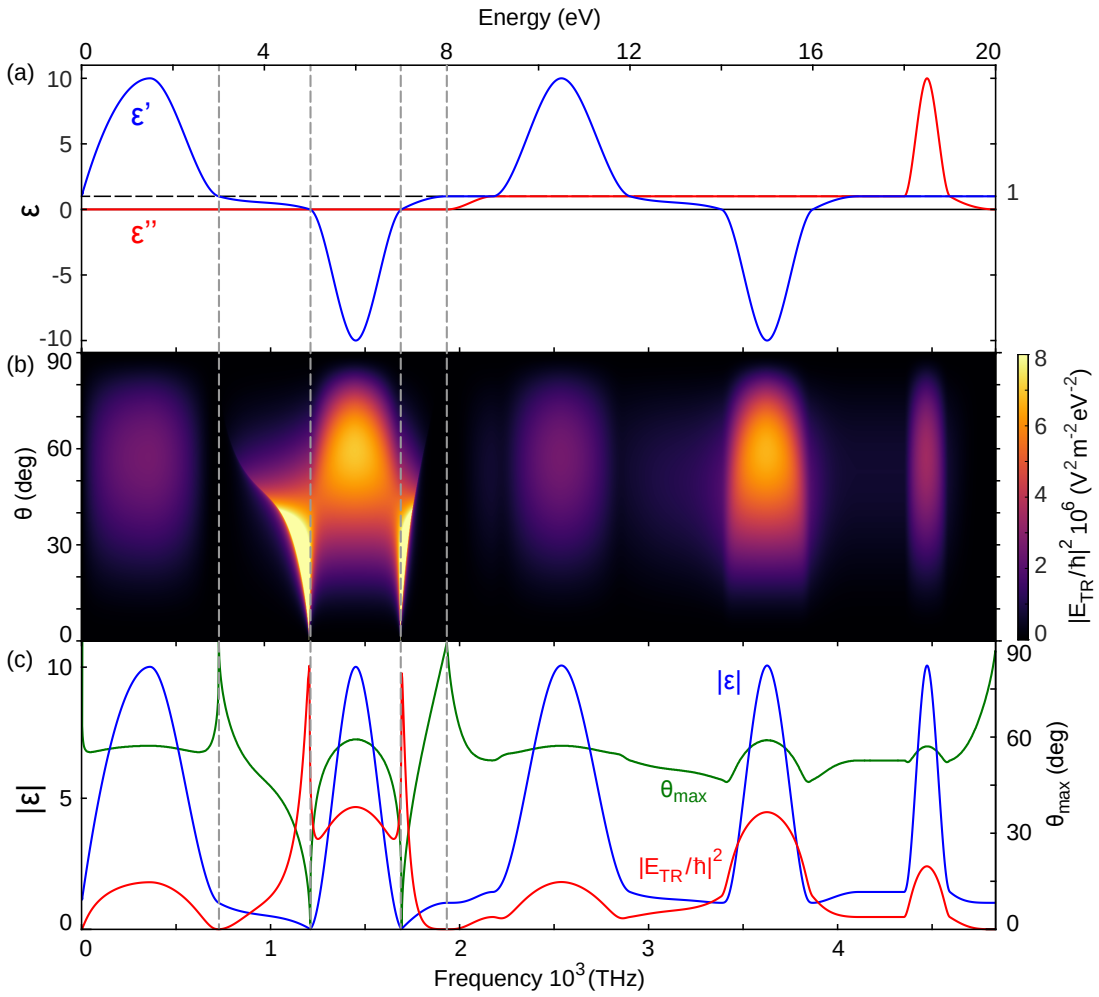

FIG. S6. Dependence of TR emission on the permittivity of an artificial material. (a) Real (ϵ', in blue) and Imaginary (ϵ", in red) parts of the artificial permittivity as a function of frequency. From left to right we use a positive and a negative peak of ϵ' for ϵ"=0 and repeat for ϵ"=1, ending with a peak in ϵ" for ϵ'=1. The horizontal dashed line denotes ϵ=1. The vertical dashed lines denote the transitions to/from regions in which the absolute value $|\epsilon| < 1$ but $\epsilon' > 0$. (b) TR electric field intensity in the frequency domain, as a function of frequency and emission angle θ for the artificial ϵ from (a). (c) Comparison of the absolute value of the artificial permittivity $|\epsilon|$ (in blue) to the normalized TR electric field intensity (in red) and the angle of maximum emission intensity θ_{max} (in green), all as a function of frequency. The TR intensity is normalized to the same maximum as $|\epsilon|$. We note that θ_{max} goes to 90° at the locations of the dashed lines, but here the intensity goes to 0, so the emission angle is not well-defined.

First, Figure S6(a) shows the real (ϵ', in blue) and imaginary (ϵ", in red) parts of the artificial permittivity, as a function of frequency. We note such a permittivity does not necessarily satisfy the Kramers–Kronig relations, but is meant to serve as an illustration. ϵ' traces out a positive and then a negative peak before becoming positive again, for ϵ"=0, before repeating the same features with ϵ"=1, finishing with a peak in ϵ" for ϵ'=1. Figure S6(b) displays the TR intensity as a function of the frequency and the emission angle. We can observe several features. First, it is clear that the peaks in negative ϵ' lead to more intense TR intensity than peaks in positive ϵ', with a factor $\sim$2 difference. Next, the peak in ϵ" shows a similar intensity to the comparable peak in positive ϵ'. All of the regions where ϵ is close to that of vacuum are very dark, since there is no longer any contrast between the two media. The most noticeable features in Figure S6(b) however, are the bright and sharp lobes that occur on both sides of the first negative peak of ϵ', which are very similar to those seen for the Drude metal in Figure 5(a). We can now see that these bright regions correspond to ranges in frequency where $1 > \epsilon' > 0$ and $\epsilon"=0$, so that $|\epsilon| < 1$. The feature becomes brighter (not visible on this color scale) and sharper at the smallest emission angles as ϵ' approaches 0, but stops quite abruptly once ϵ' becomes negative, even when $|\epsilon|$ is still below 1. Although not shown here, the edges of these features do correspond to $\theta = \arcsin(\sqrt{\epsilon})$, as was the case for the Drude metal. In the second cycle where $\epsilon"=1$, this feature has completely disappeared, which we attribute to $|\epsilon|$ no longer being smaller than 1 at any point, even when $\epsilon' < 0$. This again agrees with predictions by Stern[4], as discussed in Figure S5 and in the main text.

We examine the relation between $|\epsilon|$, the emission intensity and angle more explicitly in Figure S6(c), which is similar to Figure 6. We show $|\epsilon|$ (in blue), the total TR intensity summed over all angles (in red), normalized to the same maximum value as $|\epsilon|$, and the angle of maximum emission intensity θ_{max} (in green). Overall, we find that θ_{max} and the total intensity follow the same behavior or trend as $|\epsilon|$. The only difference occurs in the region of the bright features in Figure S6(b). For $|\epsilon|$ at or just below 1, θ_{max} exhibits a maximum, but this occurs for vanishing intensity, so this is not really significant. As $|\epsilon|$ decreases and becomes closer to 0, θ_{max} again shows the same behavior, also reaching a minimum close to 0. The total intensity however displays the opposite behavior, reaching a maximum, just as was observed in Figure 6. All of the observed behavior is consistent with the notion that TR is sensitive to the contrast between the permittivities of the two media, just as for reflection

of light. An $|\epsilon|$ much larger than 1 or much smaller than 1 ($|\epsilon|$ close to 0) both lead to very high contrast and correspondingly intense TR emission. There are however additional subtleties, such as the higher intensities for negative ϵ than for positive values, and the fact that the emission angles also track the behavior of $|\epsilon|$.

Figure S7 shows the TR emission behavior plotted explicitly as a function of ϵ, at a single energy ($\hbar\omega$=1 eV). Figure S7(a) displays the TR intensity normalized to the maximum value, as a function of ϵ' and θ, for ϵ"=0.1. The more intense TR for negative ϵ' than for positive ϵ' is clearly observed. The now familiar sharp feature for ϵ' positive but close to 0 is visible as well, but since $\epsilon" > 0$, it is relatively less bright and occurs at higher angles than in Figure S6(b). We also observe the transition region from this feature towards high intensities at higher angles for the negative values of ϵ', as well as the disappearance of emission intensity around ϵ'=1 when we lose the contrast with vacuum. In Figure S7(b), we examine the normalized TR intensity as a function of ϵ' and ϵ", for an emission angle θ=60°. We again notice the minimum in intensity around ϵ'=1 and ϵ"=0. From this minimum outwards, the intensity increases for increasing $|\epsilon|$, with again the asymmetry of enhanced emission for negative values of ϵ'. Interestingly, for negative ϵ', a higher ϵ" leads to less intensity, while for positive ϵ' a higher ϵ" leads to a very slight increase in intensity. Finally, in Figure S7(c), we show the angle of maximum emission θ_{max} as a function of ϵ' and ϵ" (note the reduced scale for the angles). The behavior of smaller emission angles for small values of $|\epsilon|$ close to 0 and increasing angles for increasing $|\epsilon|$ is confirmed. We notice that similarly to the trend in intensity, θ_{max} is larger for negative ϵ' than for positive values.

---

* polman@amolf.nl

† javier.garciadeabajo@icfo.es

[1] W. Kuhn, Z. Phys. **33**, 408 (1925).

[2] F. Reiche and W. Thomas, Z. Phys. **34**, 510 (1925).

[3] Z.-J. Yang, T. J. Antosiewicz, R. Verre, F. J. García de Abajo, S. P. Apell, and M. Käll, Nano Letters **15**, 7633 (2015).

[4] E. A. Stern, Phys. Rev. Lett. **8**, 7 (1962).

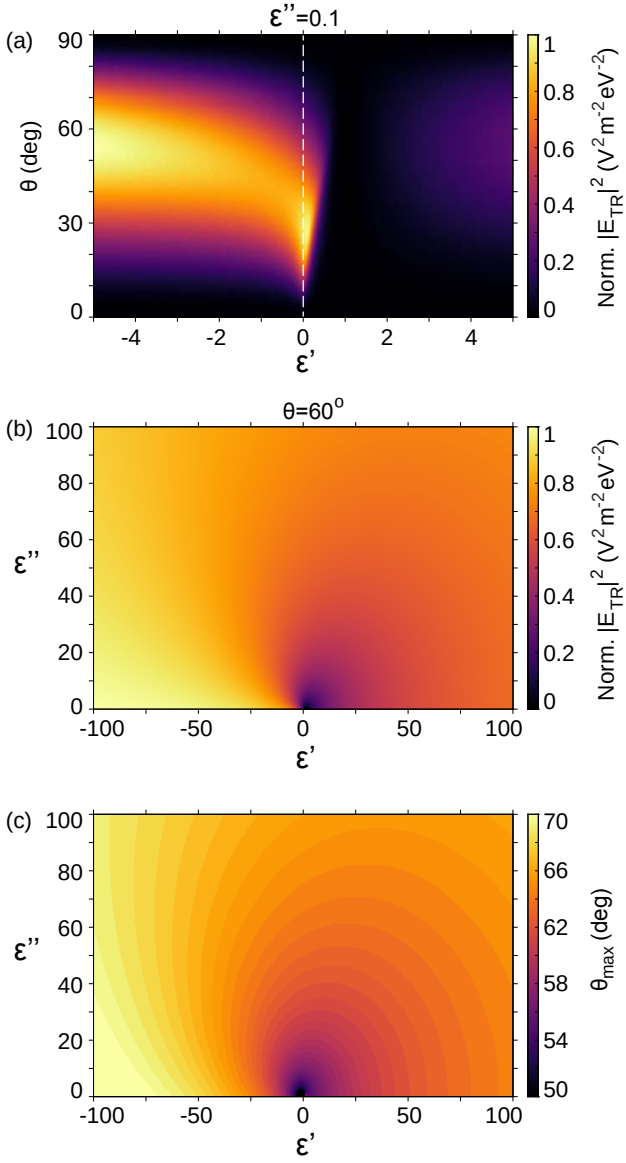

FIG. S7. Dependence of TR emission on material permittivity. (a) The TR electric field intensity in the frequency domain normalized to its maximum, as a function of ϵ' and the emission angle θ, for ϵ"=0.1. The dashed line denotes ϵ'=0. (b) The same normalized TR intensity, now shown as a function of ϵ' and ϵ" over a larger range, for θ=60°. (c) The angle of maximum emission intensity θ_{max}, as a function of ϵ' and ϵ". Note the reduced range of angles spanned by the color scale. The color steps visible in the figure are due to the discrete 0.5° steps in θ for which the calculation is performed.